A non-ordinary state-based peridynamics framework for anisotropic materials

Gabriel Hattori[a,*], Jon Trevelyan[a], William M. Coombs[a]

[a]*Department of Engineering, Durham University, DH1 3LE, Durham, UK*

Abstract

Peridynamics (PD) represents a new approach for modelling fracture mechanics, where a continuum domain is modelled through particles connected via physical interactions. This formulation allows us to model crack initiation, propagation, branching and coalescence without special assumptions. Up to date, anisotropic materials were modelled in the PD framework as different isotropic materials (for instance, fibre and matrix of a composite laminate), where the stiffness of the bond depends on its orientation. In this work we propose a non-ordinary state-based formulation to model general anisotropic materials. The material properties for each particle are defined using the material constitutive matrix, rather than being defined through the bond stiffness between adjacent particles. We propose a damage criterion for composite materials to model the crack propagation behaviour for anisotropic materials. We validate the model using benchmark problems obtained with established numerical methods or experimental results. The proposed approach enables the use of general classes of material models including rocks, concrete and biomaterials.

Keywords: peridynamics, non-ordinary state-based, anisotropic materials, crack propagation

1. Introduction

Anisotropic materials have been studied since the first works of Sih et al. [44], and ever since have attracted attention of fracture mechanics researchers. Anisotropic materials are usually brittle, almost ensuring that cracks will appear during their lifetime. The effect of cracks in an anisotropic material is more complicated than the equivalent problem with an isotropic material. For instance, the crack propagation path is also a function of the material properties, rather than depending only on the orientation of the applied load and the specimen geometry.

These materials are widely used in composites in the aerospace and automobile industries [35, 32], as sensors and actuators (piezoelectric [12, 56] and magnetoelectroelastic [30, 55] materials) and more recently have applications in biomechanics [15, 40] and even in hydraulic fracturing [16, 19], just to mention some of the works. Cracks in composite materials can be responsible for complete failure of the component, resulting in economic losses or even loss of life. Damaged smart materials exhibit different electric and magnetic fields compared to the pristine material, incurring in errors

---

*Corresponding author

Email addresses: `gabriel.hattori@durham.ac.uk` (Gabriel Hattori), `jon.trevelyan@durham.ac.uk` (Jon Trevelyan), `w.m.coombs@durham.ac.uk` (William M. Coombs)

of the response of a sensor for instance. Therefore, it is important to accurately quantify the effect
of discontinuities in anisotropic materials.

Fracture mechanics have been studied for nearly a century, from the first work of Griffith [17]
for brittle materials. Over the years a number of researchers have modelled fracture mechanics
analytically [34, 43] for simple problems and geometries, and more commonly using numerical
frameworks, such as the extended finite element method (XFEM) [4, 33] and the extended boundary
element method (XBEM) [18], among many others. Nevertheless, these methods suffer when crack
branching or coalescence are involved.

The phase-field method has been shown to model crack branching behaviour [1, 20]. The
method consists in describing the crack as an interface directly in the formulation and is used
conjointly to the finite element method (FEM) [41]. Nevertheless, the method requires a fine mesh
around the crack to model the interface correctly. Another drawback of the method is that it
can provide unrealistic results. A novel numerical method entitled peridynamics (PD) [45] has
been recently developed, and has shown great potential in fracture mechanics problems involving
initiating, propagating, branching and coalescing cracks.

The peridynamics (PD) formulation is a type of non-local formulation, where the state of a point
is measured over a finite distance. This framework was proposed by Silling [45], where he redefined
the classical approach for continuum mechanics using an integral framework considering the forces
in the bonds rather than stresses and strains as in the classical continuum mechanics. The main
reason for using this approach is that the classical formulation contains partial derivatives that
pose a challenge when dealing with fracture mechanics problems. The governing partial differential
equations in elasticity imply that singularities will appear due to the presence of discontinuities,
which is not desirable. Due to the integral form of the formulation, no special assumptions are
needed to deal with singularities, such as a crack in the domain.

The first PD formulation described a continuum medium through discrete particles, interacting
between each other through physical connections entitled bonds. Each bond has a stiffness associ-
ated with it, being analogous to a spring in continuum mechanics theory. However, each particle
has an area of influence, interacting with all other particles within a perimeter. The radius of
this perimeter is the horizon of that particle, and is a characteristic of non-local formulations (see
[11, 27] for other types of non-local approaches). The material properties in PD are calculated
using the material parameters of the classical continuum mechanics, and also parameters from PD
such as the horizon size. The tractions between different particles are in the same direction as the
bond, have opposite sense and the same magnitude. This first formulation obtained by Silling was
denoted bond-based PD.

The crack is formed when the bonds between particles are broken, a key feature of the PD
formulation. This characteristic also enables the modelling of crack initiation without further as-
sumptions. Additionally, crack branching can appear if elastic wave reflections generate instabilities
at the crack tip, which is very difficult to model in standard numerical techniques. However this
theory presented limitations with respect to the material properties. Silling has stated that the so
called bond-based PD limits the Poisson's ratio of the material (1/3 for 2D plane stress and 1/4 for
2D plane strain and 3D) [45, 47]. A more generalised framework called state-based PD has been
developed so any material properties can be assumed without restrictions [47].

The state-based PD is divided into two main approaches: the ordinary state-based PD, which
represents a generalisation of the bond-based theory, and the non-ordinary state-based PD. Some of
the main differences lie in the orientation of tractions between particles and how material properties
are obtained. The tractions in ordinary state-based PD are still in the same direction of the bond,

but they are not constrained to have the same magnitude. A relation more similar to continuum mechanics is present due to the use of state vectors. The balance of linear and angular momentum is automatically satisfied in bond-based and ordinary state-based theories, but the same is not valid for non-ordinary framework [47].

The non-ordinary theory uses non-local approximations of some of the continuum mechanics variables. This permits a more general representation of the continuum mechanics using stress-strain relations, so that the material constitutive matrix can be used, instead of calculating equivalent properties for the stiffness in the bonds as in bond-based and ordinary state-based PD. Additionally, the tractions acting on the particles are no longer constrained to the direction of the bonds nor have the same magnitude. A drawback of these properties is that the balance of linear and angular momentum are not implicitly satisfied and have to be proved. Silling et al. [47, 49] have demonstrated how these criteria can be satisfied for a specific non-ordinary state-based formulation.

Madenci and Oterkus [29] detail extensively the use of ordinary state-based PD. Warren et al. [53] and Breitenfeld et al. [5] have performed some of the first works in non-ordinary state-based PD for explicit and implicit implementations, respectively. Yaghoobi and Chorzepa [57] have modelled fibre reinforced concrete problems for non-ordinary state-based PD. Wu et al. [54] have implemented a non-ordinary state-based for the metal machining process in ductile materials, where the loss of material usually leads to instabilities due to the strain localisation problem. A simple stabilisation technique was implemented to eliminate these instabilities. Wang et al. [52] have studied crack propagation problems in rock type materials.

Some authors have investigated different anisotropic materials using PD. Hu et al. [22] and Oterkus et al. [36, 37] have implemented bond-based models for composite materials, where the fibre and the matrix have different material properties, and are defined by the orientation of the bond. However, these PD models assume only two material constants (stiffness at the bonds and in the matrix). Hu et al. [23] have also analysed delamination as well as damage in the fibre and the bonds.

Ghajari et al. [14] have implemented a bond-based model for orthotropic materials. The anisotropy is generated by changing the stiffness of the bonds with their orientation. A limitation of this model is to use only two constants to define the material properties, instead of the four used in the continuum mechanics model. Another limitation imposed by the bond-based formulation is that mode II behaviour is dependent on mode I, which is not desirable. To the best of the authors' knowledge, a general formulation for anisotropic materials in the non-ordinary state-based PD has not been found in the literature. In the current work, the material anisotropy is defined for each particle rather than being defined at the bond level. A general description of the material is possible using the proposed approach.

In this paper we propose a non-ordinary correspondence model for generally anisotropic materials for dynamic crack problems. We implement an anisotropic damage criterion in order to capture the appropriate crack propagation path. We validate our model using benchmark problems and comparison against other numerical methods or experimental results. The remainder of the paper is organised as follows: the continuum mechanics theory is briefly introduced in Section 2. We describe the state-based PD formulation in Section 3, with emphasis on the non-ordinary formulation. In Section 4, the anisotropic damage criterion is explained, while the explicit integration scheme is briefly explained in Section 5. The numerical results are presented in Section 6. The main conclusions are summarised in Section 7.

2. Classical continuum mechanics

In this section we introduce some of the parameters of continuum mechanics employed in PD. The deformation gradient characterises the behaviour of motion in the neighbourhood of a point, and it is defined as [21]

$$\mathbf{F}(\mathbf{x}) = \frac{\partial \mathbf{y}}{\partial \mathbf{x}} \tag{1}$$

where $\mathbf{x}$ denotes an arbitrary point in the reference configuration, and

$$\mathbf{y} = \mathbf{x} + \mathbf{u} \tag{2}$$

denotes a point in the deformed configuration, while $\mathbf{u}$ correspond to the displacements. The deformation gradient is in principle not symmetric. If the displacements $\mathbf{u}$ are zero, then the deformation gradient is the identity matrix.

The determinant of the deformation gradient is defined as $J = det(\mathbf{F}(\mathbf{x}))$, and this gives the ratio of the volumes between the reference and deformed configurations. Since $J > 0$, the volume of the material in the deformed configuration will never be zero. Moreover, the inverse of the deformation gradient can always be calculated.

The first Piola-Kirchhoff stress is given by [21]

$$\mathbf{P}(\mathbf{x}) = J\boldsymbol{\sigma}\mathbf{F}(\mathbf{x})^T \tag{3}$$

where $\boldsymbol{\sigma}$ stands for the Cauchy stress and the superscript T denotes the transpose of a matrix.

In the small strain assumption, the first Piola-Kirchhoff stress can be approximated by the Cauchy stress, i.e.,

$$\boldsymbol{\sigma} \approx \mathbf{P}(\mathbf{x}) \tag{4}$$

and the infinitesimal strain can be defined in terms of the deformation gradient such as

$$\boldsymbol{\varepsilon} \approx \frac{1}{2}\left(\mathbf{F}(\mathbf{x})^T + \mathbf{F}(\mathbf{x})\right) - \mathbf{I} \tag{5}$$

where $\mathbf{I}$ is the identity matrix.

In the classical continuum mechanics, the equation of motion is defined as

$$\sigma_{ij,j} + b_i(x_i, t) = \rho\ddot{u}_i \tag{6}$$

where $\mathbf{b}(\mathbf{x}, t)$ denotes the body forces per unit volume, ρ is the density and $\ddot{\mathbf{u}}$ is the acceleration.

The generalised Hooke's law is the relation between stresses and strains for an elastic material and is expressed as

$$\sigma_{ij} = C_{ijkl}\varepsilon_{kl} \tag{7}$$

where ε_{kl} are the strains, and C_{ijkl} denotes the material 4th order constitutive tensor. The most general form of anisotropy consists of 81 independent components in the constitutive tensor. Nevertheless, most anisotropic materials present symmetry properties that admit the following relations

$$C_{ijkl} = C_{jikl} = C_{ijlk} = C_{klij} \tag{8}$$

leading to a tensor with only 21 independent components for the 3D case, and 6 components in the 2D case.

Classical linear strain-displacement relations are assumed as

$$\varepsilon_{ij} = \frac{1}{2}(u_{i,j} + u_{j,i}) \tag{9}$$

4

3. State-based peridynamics

The equation of motion in state-based peridynamics (PD) is defined as [47]

$$\int_{\mathscr{H}} \{\underline{\mathbf{T}}[\mathbf{x}, t]\langle \mathbf{x}' - \mathbf{x}\rangle - \underline{\mathbf{T}}[\mathbf{x}', t]\langle \mathbf{x} - \mathbf{x}'\rangle\}dV_{\mathbf{x}'} + \mathbf{b}(\mathbf{x}, t) = \rho\ddot{\mathbf{u}}(\mathbf{x}, t) \tag{10}$$

where $\mathscr{H}$ is the family of the particle $\mathbf{x}$, while the horizon δ delimits the neighbourhood of the family of the particle of interest $\mathbf{x}$, $\mathbf{x}'$ represents the particles inside the neighbourhood of $\mathbf{x}$, $\underline{\mathbf{T}}$ is the force vector state field, and square brackets denote that the variables are taken in the state vector framework. In order for Eq. (10) to be valid, it must satisfy both balance of linear and angular momentum. The proofs can be found in [47, 49].

Silling et al. [47] have proposed a generalised peridynamics (PD) formulation, where the PD variables are expressed in terms of vector states. For instance, the reference state vector $\underline{\mathbf{X}}\langle \boldsymbol{\xi}\rangle$ is defined as

$$\underline{\mathbf{X}}\langle \boldsymbol{\xi}\rangle = \boldsymbol{\xi}, \quad \forall \boldsymbol{\xi} \in \mathscr{H} \tag{11}$$

and

$$\boldsymbol{\xi} = \mathbf{x}' - \mathbf{x} \tag{12}$$

Eq. (11) represents the mapping between all particles $\mathbf{x}'$ with respect to the particle $\mathbf{x}$. The state vector nomenclature includes an underline to make a clear distinction from matrices, while the angle brackets relate to other variables the state vector relies upon.

Another way to visualise the vector state concept is to assume a matrix form as stated in [29]. The deformation state vector $\underline{\mathbf{Y}}\langle \mathbf{x}' - \mathbf{x}\rangle$ is then defined as

$$\underline{\mathbf{Y}}\langle \mathbf{x} - \mathbf{x}'\rangle = \begin{bmatrix} \mathbf{y}_1 - \mathbf{y} \\ \mathbf{y}_2 - \mathbf{y} \\ \vdots \\ \mathbf{y}_N - \mathbf{y} \end{bmatrix} \tag{13}$$

where $\mathbf{y} = \mathbf{y}(\mathbf{x}, t)$ represents the deformed position of particle $\mathbf{x}$ at time t, and $\mathbf{y}_i = \mathbf{y}(\mathbf{x}', t)$, $i = 1, \cdots N$ denotes all the particles $\mathbf{x}'$ contained within the horizon of $\mathbf{x}$.

Figure 1 illustrates the reference (or undeformed) configuration, and the deformed configuration after a displacement $\mathbf{u}$ and $\mathbf{u}'$ has been imposed on particles $\mathbf{x}$ and $\mathbf{x}'$, respectively. Similarly, δ and δ' correspond to the horizon of particles $\mathbf{x}$ and $\mathbf{x}'$, respectively.

In the original bond-based formulation [45], the particles within the distance δ of $\mathbf{x}$ are said to be inside the horizon of that particle, thus making a contribution to the displacement solution. The bonds possess stiffness, and can be considered as springs or trusses since the bonds only have tractions in the direction of the bond. Macek and Silling [28] have used this idea to implement a bond-based formulation where the bonds were modelled by truss elements. They concluded that this formulation provided similar results to the ones found with a commercial finite element software.

However, the bond-based PD formulation presents limitations with respect to the material properties. The Poisson's ratio is restricted to $1/3$ for 2D plane stress problems and to $1/4$ for 2D plane strain and 3D problems [45], since the particles within the horizon δ' of particle $\mathbf{x}'$ are not all included during the analysis of $\mathbf{x}$. The reasons for the limitation of the Poisson's ratio are related to the fact that the equilibrium needs to be satisfied for every bond. This enforces that the forces in the bonds must be in the direction of the bond, of equal magnitude and opposite directions.
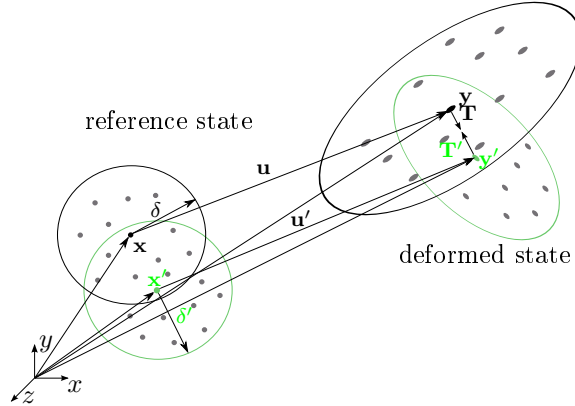
Figure 1: Reference and deformed configuration in state-based PD.

The bond-based theory assumes that the interaction between two particles is governed by a central potential that does not depend on other local conditions [47]. To overcome this limitation, Silling et al. [47] have proposed the state-based theory, which removes limitations with respect to the material properties. Other authors have developed different approaches to overcome this limitation in bond-based models (see [13] for instance). In this work, we focus on the state-based PD theory.

There are two types of state-based formulation: ordinary and non-ordinary. In the ordinary theory, the forces in the bonds are defined in the direction of the bonds, in the same way as in the bond-based formulation. However, the forces do not need to have the same magnitude, as in the bond-based approach. On the other hand, the non-ordinary formulation presents no restriction with respect to the direction of the bond and the magnitude of the tractions. These differences are illustrated in Figure 2.
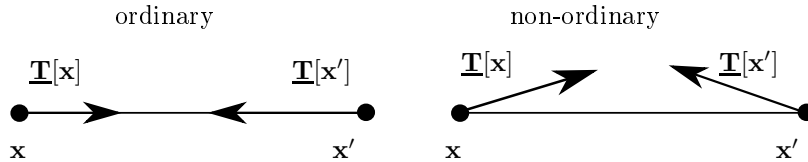

Figure 2: Differences between traction in the bonds in ordinary and non-ordinary state-based PD.

The process of obtaining the equivalent material properties in the ordinary state-based formulation is not straightforward. There are no direct equivalences of stresses and strains in the ordinary framework. In this sense, a typical approach is to draw an equivalence between the strain energy for the continuum mechanics theory and the strain energy density in the PD framework. Then the material properties are obtained by solving a series of simple problems with known deformation, such as pure shear, uni-axial deformation, bi-axial deformation [29]. For isotropic materials or some specific anisotropic (e.g. orthotropic) materials, analytical solutions can be obtained. However, analytical solutions are not possible for generally anisotropic materials.

The equivalence between strain energy densities from continuum mechanics and PD framework also poses another inconvenience. Particles closer to the boundaries of the analysed domain will share bonds with fewer particles than those in the middle of the domain, for example. However,

165 it is assumed that the strain energy density for the particles, regardless of the number of particles in the horizon, leading to an overestimation of the material properties at the boundaries [29, 50]. Correction factors have been proposed to modify the strain energy for a particle whose horizon contains a reduced number of particles (see [24] for a detailed explanation on different techniques).

3.1. Non-ordinary state-based PD

170 The non-ordinary PD framework is a more generalised approach, where some of the main parameters in continuum mechanics, such as the deformation gradient, are expressed in terms of the PD formulation. Since these parameters are not constrained by the physical bonds connecting the particles, the tractions in the bonds are not enforced to be in the same direction as the bonds themselves, as is the case in ordinary PD models. Another advantage is that the material properties in

175 the non-ordinary state-based formulation come from the material constitutive matrix, which is not the case for the ordinary state-based PD.

The deformation gradient $\mathbf{F}(\mathbf{x})$ in the classical continuum mechanics is given by Eq. (1). The non-local deformation gradient $\mathbf{F}(\mathbf{x})$ for each particle is given by [47]

$$\mathbf{F}(\mathbf{x}) = \left[\int_{\mathscr{H}} \omega(|\xi|)(\underline{\mathbf{Y}}(\xi) \otimes \xi)dV_{\mathbf{x}} \right].\mathbf{B}(\mathbf{x}) \tag{14}$$

$$\mathbf{B}(\mathbf{x}) = \left[\int_{\mathscr{H}} \omega(|\xi|)(\xi \otimes \xi)dV_{\mathbf{x}} \right]^{-1} \tag{15}$$

where $\mathbf{B}(\mathbf{x})$ is the shape tensor, $\otimes$ denotes the dyadic product of two vectors, and $\omega(|\boldsymbol{\xi}|)$ is a dimensionless weight function, used to increase the influence of the nodes closes to $\mathbf{x}$. In this work, we assumed that the influence function has a triangular shape, and is given by

$$\omega(|\boldsymbol{\xi}|) = 1 - \frac{\xi}{\delta} \tag{16}$$

where $\xi = |\boldsymbol{\xi}|$. The reason for using this influence function is to make the behaviour of particles closer to $\mathbf{x}$ more dominant than the ones more distant. Warren et al. [53] have used a unitary influence function, while Queiruga and Moridis [39] have investigated several influence functions for

180 simple problems in 2D and concluded that the triangular function given by Eq. (16) leads to lower errors for the non-ordinary state-based PD.

The discretisation of Eqs. (14) and (15) can be expressed as a Riemann sum as [53]

$$\mathbf{F}(\mathbf{x}_j) = \left[\sum_{n=1}^{m} \omega(|\mathbf{x}_n - \mathbf{x}_j|)(\underline{\mathbf{Y}}\langle \mathbf{x}_n - \mathbf{x}_j \rangle \otimes (\mathbf{x}_n - \mathbf{x}_j))V_n \right].\mathbf{B}(\mathbf{x}_j) \tag{17}$$

$$\mathbf{B}(\mathbf{x}_j) = \left[\sum_{n=1}^{m} \omega(|\mathbf{x}_n - \mathbf{x}_j|)((\mathbf{x}_n - \mathbf{x}_j) \otimes (\mathbf{x}_n - \mathbf{x}_j))V_n \right]^{-1} \tag{18}$$

where m is the number of particles with the horizon of node j and V_n is the volume of particle n. Let us remark that each particle $\mathbf{x}_j$ must be connected to at least two other particles in different orientations to ensure that $\mathbf{B}(\mathbf{x}_j)$ will not be singular for 2D problems. To illustrate this behaviour, let us consider a particle $\mathbf{x}_j = (a, c)$ and its interaction with $\mathbf{x}_n = (b_n, c), n = 1 \cdots M$ which

7

represent the other particles in this family, with $a, b_n, c \neq 0$. All particles are in the same line. For a 2D problem, the shape tensor is given by

$$\mathbf{B}(\mathbf{x}_j) = \left[\sum_{n=1}^{M} \omega(|\mathbf{x}_n - \mathbf{x}_j|) \left[\begin{array}{cc} b_n - a & 0 \\ 0 & 0 \end{array} \right] \right]^{-1} \quad (19)$$

It is clear that the inverse of this matrix does not exist, leading to the aforementioned singular behaviour of the shape tensor. This analysis is valid for any family where the particles share the same coordinate in either x or y-direction. The same analogy is valid for 3D problems, where at least three particles in different planes must be connected to avoid singularity of $\mathbf{B}(\mathbf{x}_j)$. This issue was first reported by Warren et al. [53] for 3D problems.

According to [47], a material is denominated simple if the traction state depends only on the deformation state, i.e., $\underline{T} = \underline{\mathbf{T}}(\underline{\mathbf{Y}})$. A material is simple and elastic if the traction state can be expressed as

$$\underline{\mathbf{T}} = \nabla W(\underline{\mathbf{Y}}) \quad (20)$$

where W is the strain energy density and ∇ represents the Fréchet derivative.

The force and deformation can be related in a state vector framework by using a stress-strain model as an intermediate step [48]. For a strain energy density $W(\mathbf{F})$, the stress tensor can be expressed as [53]

$$\underline{\mathbf{T}} = \nabla W = \frac{\partial W}{\partial \mathbf{F}} \nabla \mathbf{F} \quad (21)$$

The transpose of the first Piola-Kirchhoff stress is a measure of the derivative of the strain energy density W with respect to the deformation gradient, i.e.

$$\mathbf{P}(\mathbf{x})^T = \frac{\partial W}{\partial \mathbf{F}} \quad (22)$$

Substituting Eq. (22) into Eq. (20) and evaluating the Fréchet derivative, the traction state is defined explicitly as

$$\underline{\mathbf{T}}[\mathbf{x}, t]\langle \mathbf{x}' - \mathbf{x} \rangle = \omega(|\mathbf{x}' - \mathbf{x}|)\mathbf{P}(\mathbf{x})^T . \mathbf{B}(\mathbf{x}).(\mathbf{x}' - \mathbf{x}) \quad (23)$$

Let us remark that there is no dependence on time for $\mathbf{P}(\mathbf{x})$ and $\mathbf{B}(\mathbf{x})$, however these parameters are modified when bonds are broken.

The processing of mapping a stress tensor as a peridynamic force state is the inverse of the process of approximating the deformation state by a deformation gradient tensor. A peridynamic constitutive model that uses stress as an intermediate quantity results in general in bond forces which are not parallel to the deformed bonds [47].

In this work the material anisotropy is considered through Eq. (7), where the anisotropic material constitutive matrix can be employed in the non-ordinary state-based framework. The material properties are thus defined for each particle, rather than being defined through the stiffness of the bond connecting two particles. This enables the use of general material models in non-ordinary state-based PD. An issue of the bond-based and ordinary state-based theories is that modelling anisotropic materials can be complicated because the bonds direction may not be aligned with the material orientation. This restricts the class of anisotropic materials that can be modelled within these frameworks, for example, materials that present some symmetries such as orthotropic materials. It is cumbersome to define the stiffness of each bond for a general anisotropic material model within the bond-based framework.

8

4. Damage criterion for anisotropic materials

In PD, damage is modelled through the bond breakage between pairs of particles. Once a bond is broken, the interaction between particles provided by that bond will not be used during the rest of the analysis. A damage index $\varphi(\mathbf{x}, t)$ is used to measure the relation of damaged bonds and active bonds for any given particles and is given by

$$\varphi(\mathbf{x}, t) = 1 - \frac{\int_{\mathscr{H}} \mu(\boldsymbol{\xi}, t) dV_\xi}{\int_{\mathscr{H}} dV_\xi} \tag{24}$$

and

$$\mu(\boldsymbol{\xi}, t) = \left\{ \begin{array}{ll} 1 & \text{if the bond is active} \\ 0 & \text{if the bond is broken} \end{array} \right. \tag{25}$$

From Eq. (24), $0 \leq \varphi(\mathbf{x}, t) \leq 1$, where 0 represents the undamaged state and 1 represents the breakage of all the bonds of a given particle. The parameter $\mu(\boldsymbol{\xi}, t)$ is used only to specify if a particular bond is active or broken. The broken bonds will eventually lead to a softening material response, since failed bonds cannot sustain any load.

There are different damage criteria for anisotropic materials. For instance, Pensée et al. [38] have considered a micromechanical approach for modelling damage in anisotropic brittle materials such as rocks and concrete, based on energy and a multiscale approach. The damage criterion is related to the type of anisotropic material analysed. In this work, we have employed the Tsai-Hill criterion to define damage in the bonds. This criterion is used for composite laminates and can take into account failure between different modes and is given by the following expression

$$\left(\frac{\sigma_L}{\sigma_{Lu}} \right)^2 + \left(\frac{\sigma_T}{\sigma_{Tu}} \right)^2 - \frac{\sigma_L}{\sigma_{Lu}} \frac{\sigma_T}{\sigma_{Lu}} + \left(\frac{\tau_{LT}}{\tau_{LTu}} \right)^2 = 1 \tag{26}$$

where σ_L, σ_T and τ_{LT} stand for the longitudinal stress (in the direction of the fibre), transversal stress (perpendicular to the fibre) and shear stress, respectively. σ_{Lu}, σ_{Tu} and τ_{LTu} are the respective tensile strength of the composite material for different loading.

In order to use this criterion in PD, the stress in a bond is defined as the average stress between the interacting particles, such as

$$\sigma(\mathbf{x}, \mathbf{x}') = \frac{1}{2} \left(\sigma(\mathbf{x}) + \sigma(\mathbf{x}') \right) \tag{27}$$

In this case, we can employ the Cauchy stresses instead of the first Piola-Kirchhoff stress since we are using the small strain assumption.

Next, the stress at the bond is expressed in terms of a local coordinate system using the rotation matrix $\mathbf{R}(\theta)$, which depends on the fibre orientation θ and is defined as

$$\mathbf{R}(\theta) = \left[\begin{array}{ccc} \cos^2 \theta & \sin^2 \theta & 2 \cos \theta \sin \theta \\ \sin^2 \theta & \cos^2 \theta & -2 \cos \theta \sin \theta \\ -\cos \theta \sin \theta & \cos \theta \sin \theta & \cos^2 \theta - \sin^2 \theta \end{array} \right] \tag{28}$$

Figure 3 illustrates the rotation with the global and local stresses, with respect to the fibre orientation.
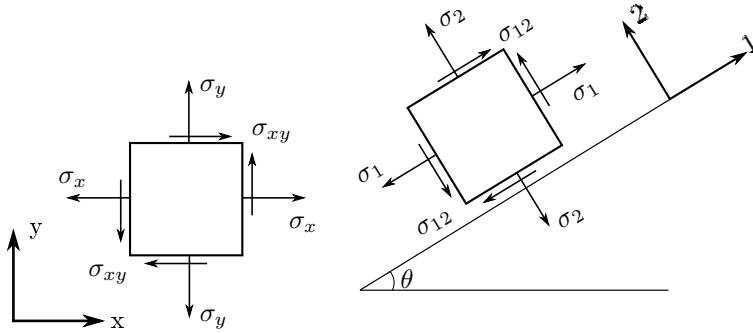
9

Figure 3: Rotation of the stresses from global (x,y) to local (1,2) coordinates.

Finally, the local stresses are given by

$$
\begin{bmatrix} \sigma_L \\ \sigma_T \\ \tau_{LT} \end{bmatrix} = \mathbf{R}(\theta) \begin{bmatrix} \sigma_{xx} \\ \sigma_{yy} \\ \tau_{xy} \end{bmatrix} \tag{29}
$$

where σ_{xx}, σ_{yy} and τ_{xy} are the stresses in the global coordinate system. The local stresses of Eq. (29) are combined into Eq. (26), and if the result is higher than 1, then the current bond breaks.

Let us remark that different criteria have been used for non-ordinary state-based PD. For instance, Wang et al. [52] and Zhou et al. [59] have used a stress criterion to model damage in rocks using a linear Mohr-Coulomb failure criterion, but they consider the rock to be an isotropic material. To the authors' knowledge, this is the first time that a damage criterion for composite materials is employed within a non-ordinary state-based PD framework. It shows that different damage criteria for anisotropic materials can be employed in the future.

5. Numerical discretisation

In this work, an explicit integration scheme was employed to calculate the displacements, velocities and accelerations in the PD framework, in a similar way as in the work of [53]. A drawback of the PD formulation is the requirement for a large computational power, since a large number of particles are typically used. In order to reduce the extensive computational calculations, some authors have tried to tackle this issue by coupling PD with standard numerical methods, such as the FEM [25, 58]. Moreover, each particle interacts with a number of other particles, which contributes for the method to be computationally expensive. However, a parallel implementation of a PD explicit formulation is straightforward with OpenMP or MPI for instance. In this work we have implemented the non-ordinary state-based formulation in a Fortran 90 code, then used OpenMP to improve computational performance. Although not done in the current work, numerical calculations in PD are also suitable to be implemented using GPUs, as have been performed by [31] with OpenCL and OpenMP and [26] using OpenACC.

For the small strain assumption, the infinitesimal strain state can be approximated by Eq. (5) and the Cauchy stresses $\boldsymbol{\sigma}$ are evaluated using Eq. (7).

The values of acceleration are calculated directly from Eq. (10). The velocities are integrated using a forward difference approach, while the displacements are obtained through a backward

10

scheme. The numerical integration is summarised by

$$\ddot{\mathbf{u}}(\mathbf{x},t) = \frac{1}{\rho}\left(\int_{\mathscr{H}}\{\underline{\mathbf{T}}[\mathbf{x},t]\langle\mathbf{x}'-\mathbf{x}\rangle - \underline{\mathbf{T}}[\mathbf{x}',t]\langle\mathbf{x}-\mathbf{x}'\rangle\}dV_{\mathbf{x}'} + \mathbf{b}(\mathbf{x},t)\right) \tag{30}$$

$$\dot{\mathbf{u}}(\mathbf{x},\Delta t + t) = \dot{\mathbf{u}}(\mathbf{x},t) + \ddot{\mathbf{u}}(\mathbf{x},t)\Delta t \tag{31}$$

$$\mathbf{u}(\mathbf{x},\Delta t + t) = \mathbf{u}(\mathbf{x},t) + \dot{\mathbf{u}}(\mathbf{x},t)\Delta t \tag{32}$$

where $\dot{\mathbf{u}}(\mathbf{x},t)$ are the velocities and $\mathbf{u}(\mathbf{x},t)$ are the displacements.

Due to the use of an explicit approach, the time step must be smaller than a certain critical value in order for the analysis to be valid. Silling and Askari [46] and Madenci and Oterkus [29] have obtained the critical time step for bond-based and ordinary state-based theories, respectively. Warren et al. [53] have used the Courant-Friedrichs-Lewy condition [7] to estimate the critical time step for a non-ordinary state-based PD. In this case, the critical time step is proportional δ/c_p, where $c_p = \sqrt{C_{22}/\rho}$ is the dilatational wave speed and $C_{22} = C_{2222}$. We used a conservative approach to guarantee a time step size smaller than the critical value. In this work we assumed $\Delta t = 0.01\frac{\delta}{c_p}$.

Let us remark that some authors have proposed modifications to improve the numerical calculation in PD. For instance, Seleson [42] has provided a detailed study on different techniques to evaluate the area of the neighbourhood of a particle. In this work we found that the error due to the approximation of the area of influence of a single particle is negligible, and therefore we do not impose a volume correction.

6. Numerical simulations

In this section we investigate several applications for the PD formulation in anisotropic materials for 2D problems. The dynamic stress intensity factors (DSIF) are calculated and compared with converged FEM solutions. We have employed the extrapolation method in order to calculate the DSIF as follows [18, 56]

$$\left(\begin{array}{c} K_{II}(t) \\ K_I(t) \end{array}\right) = \sqrt{\frac{\pi}{8\overline{r}}}(\Re(i\mathbf{A}\mathbf{B}^{-1}))^{-1}\left(\begin{array}{c} \Delta u_1(t) \\ \Delta u_2(t) \end{array}\right) \tag{33}$$

where $K_I(t)$ and $K_{II}(t)$ are the dynamic mode I and mode II at time t, respectively; $\Delta u_1(t)$ and $\Delta u_2(t)$ are the crack opening displacement at time t in the x and y-direction, respectively; $\mathbf{A}$, $\mathbf{B}$ come from the material properties and are obtained from the Stroh formalism [18, 51]; $\Re(\cdot)$ represents the real part of $(\cdot)$ while i is the imaginary component; and $\overline{r}$ is the distance where the crack opening displacements are measured to the crack tip.

Note that in the present work DSIF calculations are performed only for analyses that do not consider crack propagation. We perform this computation in order to assess the dynamic behaviour of the anisotropic materials.

6.1. Edge crack in an anisotropic 2D plate

A square plate containing an edge crack is analysed in this section. The plate has dimensions $h = w = 0.1$ m, and the length of the crack is $a = 0.05$ m. Figure 4 illustrates this example. The plate is a symmetric angle ply composite laminate of four graphite-epoxy laminae, with the following material properties: $E_1 = 144.8$ GPa, $E_2 = 11.7$ GPa, $G_{12} = 9.66$ GPa and $\nu_{12} = 0.21$.

11

The density was assumed to be $\rho = 2710$ kg/m^3. The material constitutive matrix $\mathbf{C}_{IJ}$ in Voigt notation is calculated as

$$\mathbf{C}_{IJ} = \begin{pmatrix} 1/E_1 & -\nu_{12}/E_1 & 0 \\ -\nu_{12}/E_1 & 1/E_2 & 0 \\ 0 & 0 & 1/G_{12} \end{pmatrix}^{-1} \tag{34}$$

The material properties have been rotated by an angle θ ranging from 0° to 90° in order to evaluate the effect in the corresponding SIFs. The rotation of the constitutive matrix is given by

$$C_{ijkl} = r_{im}(\theta)r_{jn}(\theta)r_{ko}(\theta)r_{lm}(\theta)C_{mnop} \tag{35}$$

where C_{mnop} is the unrotated material properties, C_{ijkl} is the rotated one and

$$r_{ij}(\theta) = \begin{pmatrix} \cos\theta & \sin\theta \\ -\sin\theta & \cos\theta \end{pmatrix} \tag{36}$$

is the rotation matrix.

The plate is subjected to an initial velocity field in the y-direction and it is defined as

$$\dot{u}(\mathbf{x}, t) = \frac{\partial u(\mathbf{x}, 0)}{\partial t} = 50 \frac{y}{2h} \text{m/s} \tag{37}$$
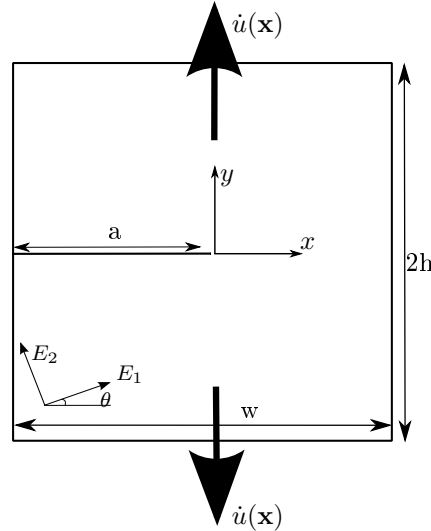

Figure 4: Anisotropic edge crack.

Some authors have investigated how the non-local PD theory converges to other non-local formulations, or even local ones. A detailed explanation of the main branches of this research field are given in [9]. Bobaru et al. [3] studied the convergence in PD for 1D problems, and concluded that there are three main different approaches:

1. $m-$convergence: the number of particles m increases as the horizon remains fixed. The PD converges to the non-local solution for that particular horizon;

12

2. $\delta-$convergence: $\delta \to 0$ while m is fixed. In this case the PD formulation converges to the local solution, i.e., the solution obtained with FEM for instance;

3. $\delta m-$convergence: the number of particles m increases as $\delta \to 0$, with m increasing faster than δ decreases. The solution converges uniformly to the local solution and faster than using the $m-$ convergence alone.

Initially we investigate how the horizon size influences the DSIF for an anisotropic material. The material orientation is fixed at $\theta = 30°$ and we calculate the DSIF for different horizon sizes. The dynamic mode I and mode II stress intensity factors are given in Figures 5 and 6 for four different particle discretisations. In all cases the DSIFs obtained with PD are compared with those obtained using a 500×500 4-node fully integrated quadrilateral finite element mesh. The horizon is defined as $\delta = m\Delta x$, where m is a constant and Δx is the grid spacing.
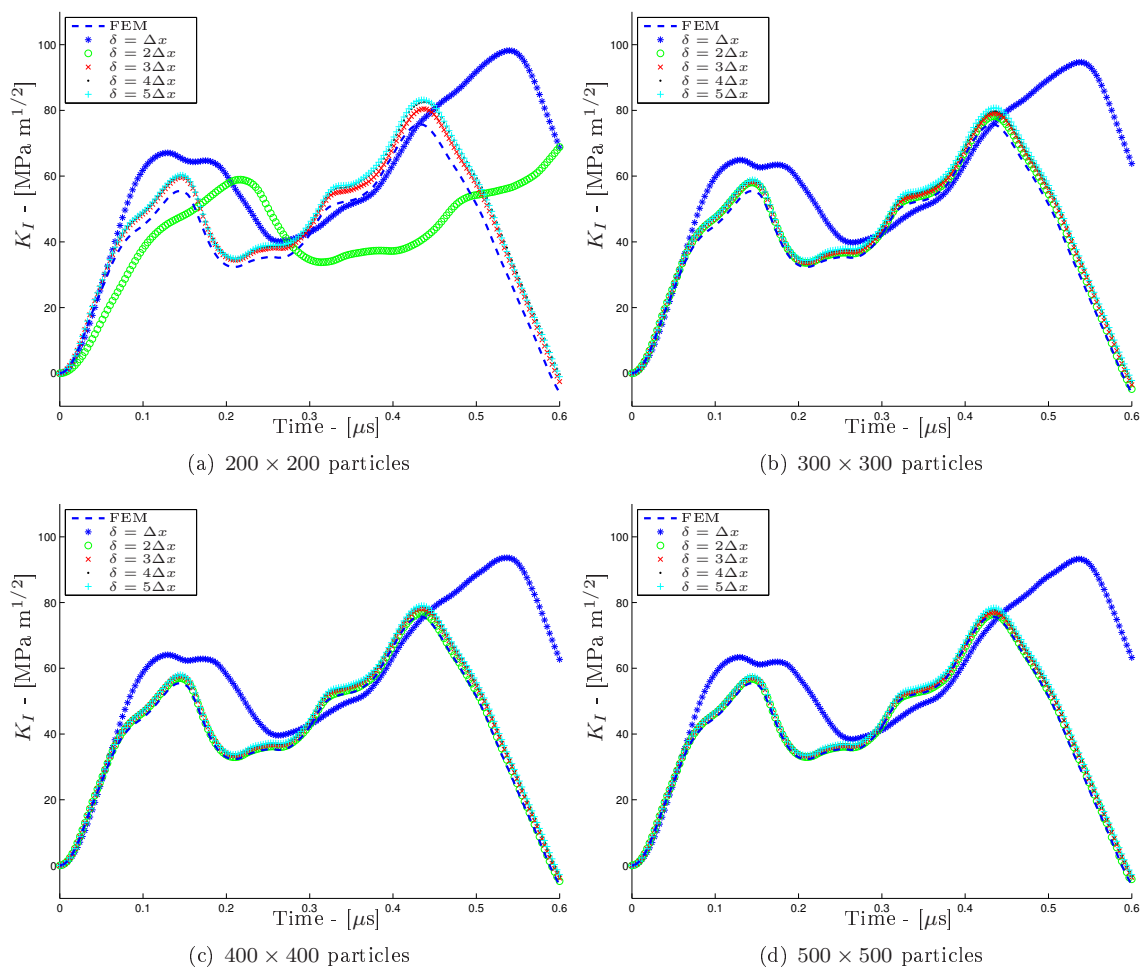

(a) 200×200 particles

(b) 300×300 particles

(c) 400×400 particles

(d) 500×500 particles

Figure 5: Edge crack: comparison different grid spacing and horizon size - mode I.

13

(a) 200×200 particles

(b) 300×300 particles

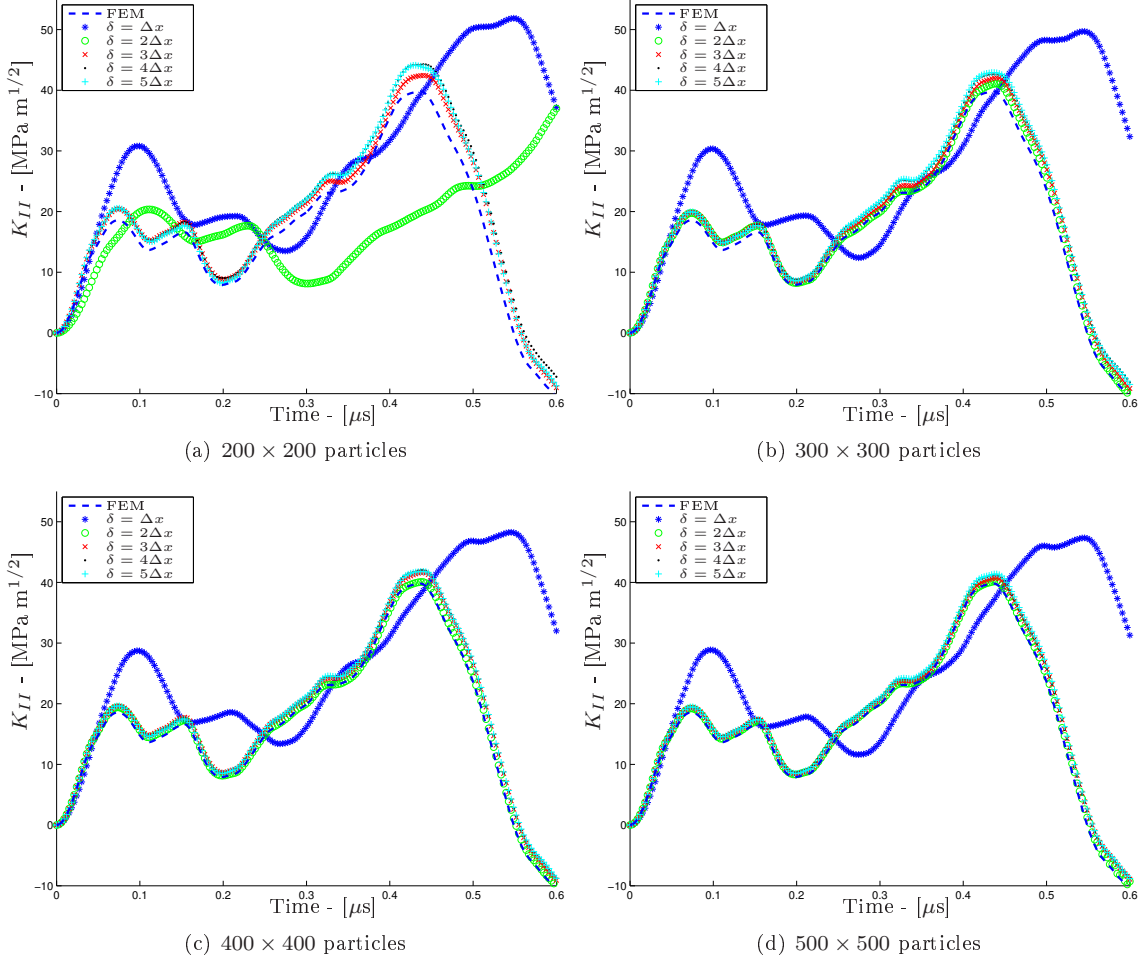(c) 400×400 particles

(d) 500×500 particles

Figure 6: Edge crack: comparison different grid spacing and horizon size - mode II.

Table 1 shows the comparison between the PD and FEM solutions. The error in the L_2 norm is calculated as

$$\text{Error} = \frac{\sqrt{\sum_{i=1}^{N}(K_{\alpha_i}^{PD} - K_{\alpha_i}^{FEM})^2}}{\sqrt{\sum_{i=1}^{N}(K_{\alpha_i}^{FEM})^2}} \tag{38}$$

where N is the total number of time steps, K_α^{PD} and K_α^{FEM} are the DSIFs for the PD and FEM formulations, respectively, and $\alpha = I, II$.

In Figure 5(a), the DSIFs calculated for $m = 1$ and $m = 2$ are in total disagreement with the reference FEM solution and the other PD solutions as well. This is due to the fact that the dynamics are not modelled properly in this case; the horizon size is not adequate for this particular grid spacing. When the grid spacing decreases, the quality of the solution calculated with smaller horizon sizes also increases, agreeing with the reference solution, as can be seen in Figure 5(b), where

14

Table 1: Relative error between PD and FEM for the dynamic mode I.

Particles	Δx (m)	Horizon $\delta = m\Delta x$				
		$m = 1$	$m = 2$	$m = 3$	$m = 4$	$m = 5$
200×200	5.0×10^{-4}	0.9898	0.7387	0.1137	0.1643	0.1374
300×300	3.3×10^{-4}	0.9317	0.0520	0.0861	0.1122	0.1130
400×400	2.5×10^{-4}	0.8990	0.0273	0.0751	0.0844	0.0847
500×500	2.0×10^{-4}	0.8808	0.0306	0.0580	0.0654	0.0719

the error solution for $m = 2$ decreases from 0.7387 to 0.0520, representing a better correlation to the reference solution, while $m = 1$ shows a small reduction in the error but still provides a poor approximation. In Figures 5(c) and 5(d), there are negligible differences between the DSIFs obtained with PD for any horizon size. The same analysis is valid for the dynamic mode II results depicted in Figure 6.

From the previous analysis and the results from Table 1, we adopt the following parameters: 400×400 particle discretisation and $m = 2$, as this has the lowest error between the FEM and PD solutions. Next we evaluate the DSIF for these parameters and varying the anisotropy angle θ. The dynamic mode I and II stress intensity factors are shown in Figures 7 and 8, respectively. An excellent agreement is obtained for the PD solution compared to a FEM approach.
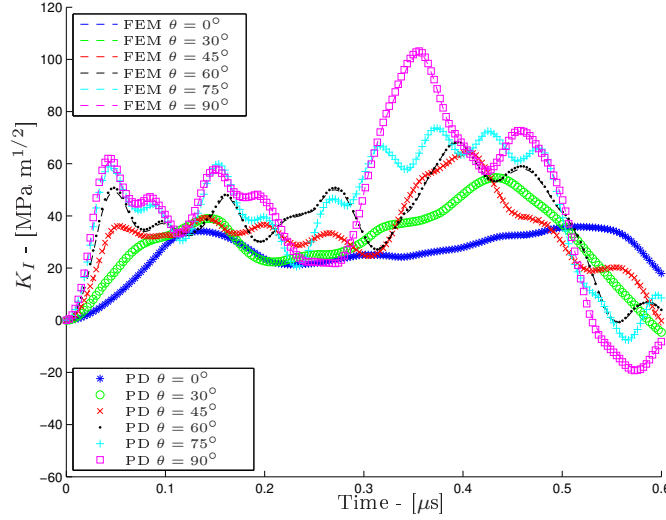

Figure 7: Edge crack: DSIF for different values of θ - mode I.

6.2. Crack propagation of centred crack in anisotropic 2D plate

In this section we analyse the crack propagation in an anisotropic rectangular plate as depicted in Figure 9. The plate has aspect ratio $h/w = 2$ and contains a centred crack such that $a/w = 0.2$. The plate has dimensions $w = h = 125$ mm. The plate is made from a unidirectional HTA/6376 composite laminate and the material properties are given in Table 2, with $G_{12} = 5.5$ GPa, $\sigma_{LTu} = 70$ MPa and $\nu_{12} = 0.3$. The plate is subjected to an initial velocity gradient $\dot{u}(\mathbf{x}, 0) = 50\frac{y}{2h}$ m/s.
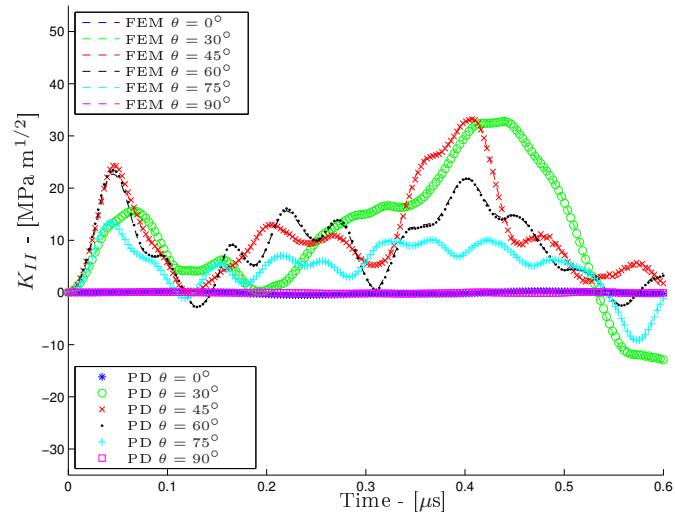
Figure 8: Edge crack: DSIF for different values of θ - mode II.
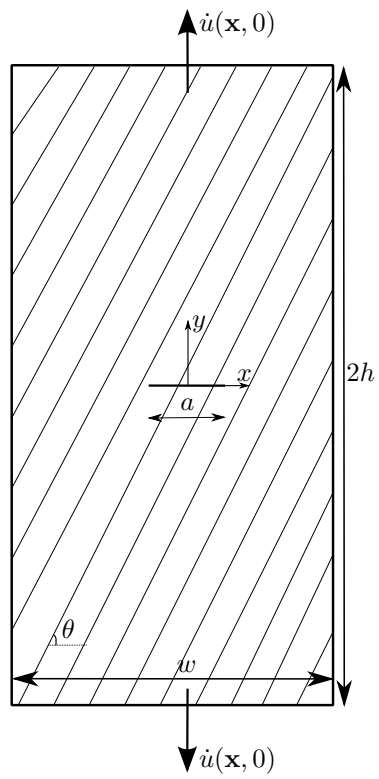

Figure 9: Anisotropic plate with centred crack.

Table 2: Material properties of HTA/6376 composite

	HTA fibre	6376 epoxy	laminate ($\theta = 0°$)	laminate ($\theta = 90°$)
Young's modulus [GPa]	235	3.6	136	8.75
Tensile strength [MPa]	3920	105	1670	60
Maximum elongation	1.7%	3.1%	-	-
Density [kg/m³]	1770	1310	1586	1586

We study the effect of the particle discretisation and the horizon size for $\theta = 45°$. Cahill et al. [6] give experimentally found paths of crack propagation in unidirectional composite materials. They have shown that the crack propagation path grows parallel to the fibre direction, indicating that the damage originates only through matrix failure. Figures 10, 11 and 12 illustrate the crack propagation for different grid spacing and horizon sizes. Only the region around the crack is represented. The Figures represent the damage index φ for the deformed configuration, where blue stands for $\varphi = 0$ while the red colour stands for $\varphi = 1$. The displacements are scaled by a factor of 20.

It is clear that for $m = 2$, the crack path is irregular and some branching can occur at the crack tips. One reason for this behaviour is that the energy of a broken bond is redistributed to the remaining active bonds in that particle, which also lead these bonds to break. Hence, a larger horizon will stabilise the crack propagation, since there are more particles to re-balance the energy from broken bonds. Similar conclusions were reached by [8] for simpler bond-based PD models of isotropic media. However, larger horizon in coarse particle discretisation can lead to problematic results. Some oscillations and crack nucleation sites are visible at the edges of the plate, and these are attributed to the dynamics of the problem as the crack approaches the edge of the plate. However, as illustrated in Figures 10(c), 10(d) and 11(d), this effect takes place too early for the coarse discretisations and is presenting an unrealistic result. Moreover, $m = 3$ and $m = 4$ seem to provide stable results for the 300×600 discretisation, shown in Figures 11(b) and 11(c), and 400×800 discretisation illustrated in Figures 12(b) and 12(c). The suggested remedy proposed by [8] of increasing m to 6-7 to stabilise the crack propagation path may give rise to inaccuracies in representing the elastic wave propagation, since the wave speed will spuriously increase with increasing horizon.

(a) $m = 2$ (b) $m = 3$ (c) $m = 4$ (d) $m = 5$
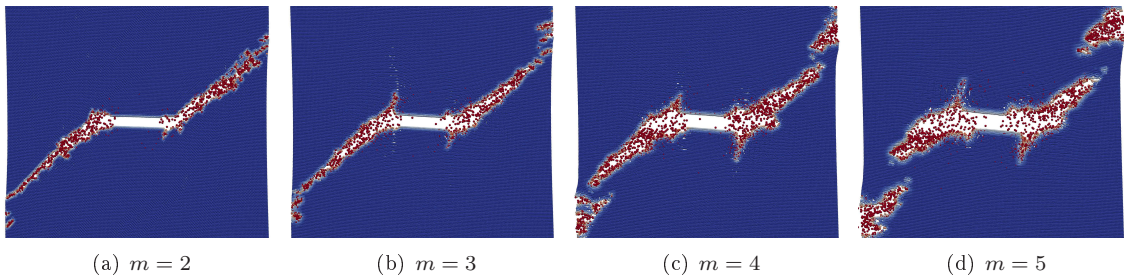
Figure 10: Crack propagation of centred crack for different horizon - $\theta = 45°$ - 200×400 particles.

Figures 13, 14, 15 and 16 illustrate different fibre orientations for $m = 3$ and 300×600 particle discretisation. The crack propagation paths are compared with experimental ones from [6] for uni-directional HTA/ 6376 composite.
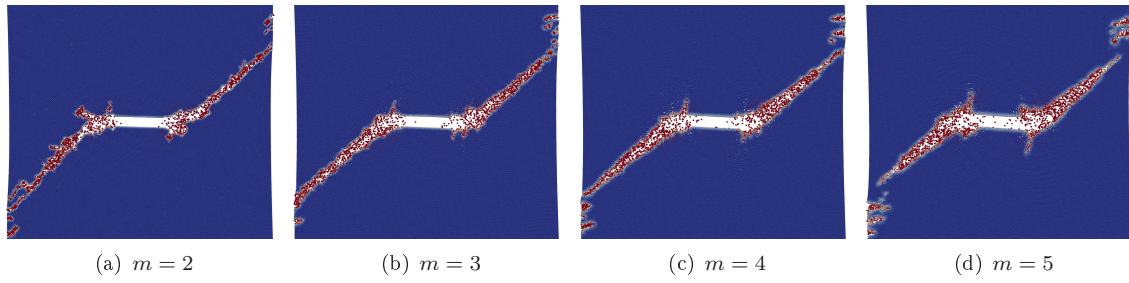
17

(a) $m = 2$

(b) $m = 3$

(c) $m = 4$

(d) $m = 5$

Figure 11: Crack propagation of centred crack for different horizon - $\theta = 45°$ - 300×600 particles.

(a) $m = 2$

(b) $m = 3$

(c) $m = 4$

(d) $m = 5$
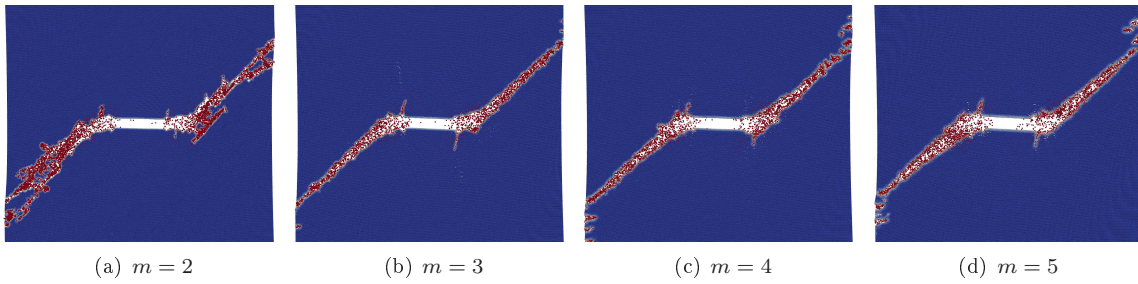
Figure 12: Crack propagation of centred crack for different horizon - $\theta = 45°$ - 400×800 particles.

(a) $t = 14.08\mu s$

(b) $t = 23.46\mu s$

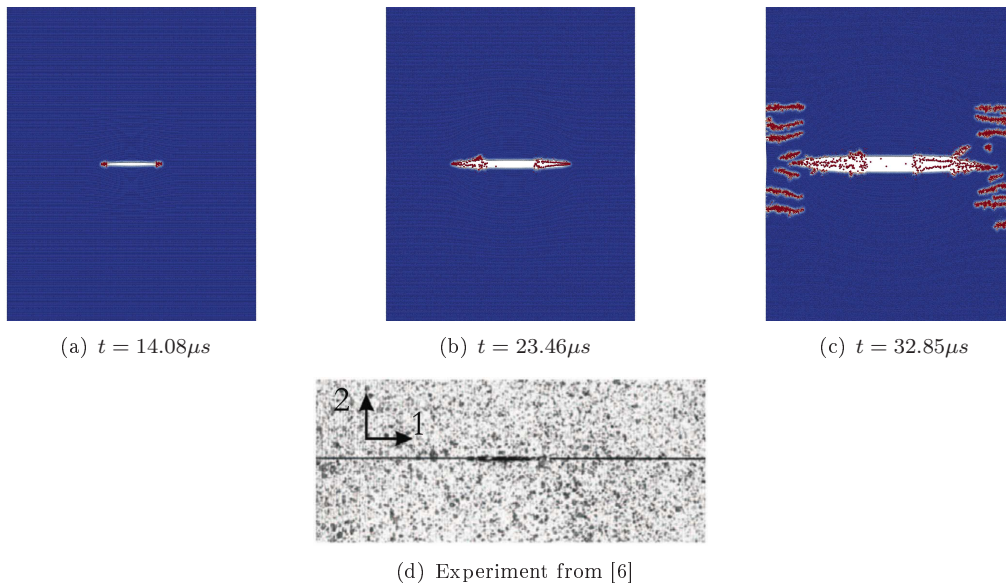(c) $t = 32.85\mu s$

(d) Experiment from [6]

Figure 13: Crack propagation of centred crack for $\theta = 0°$ - $m = 3$ - 300×600 particles.

330   From Figures 13 to 16, the crack propagation paths in PD match those obtained experimentally.
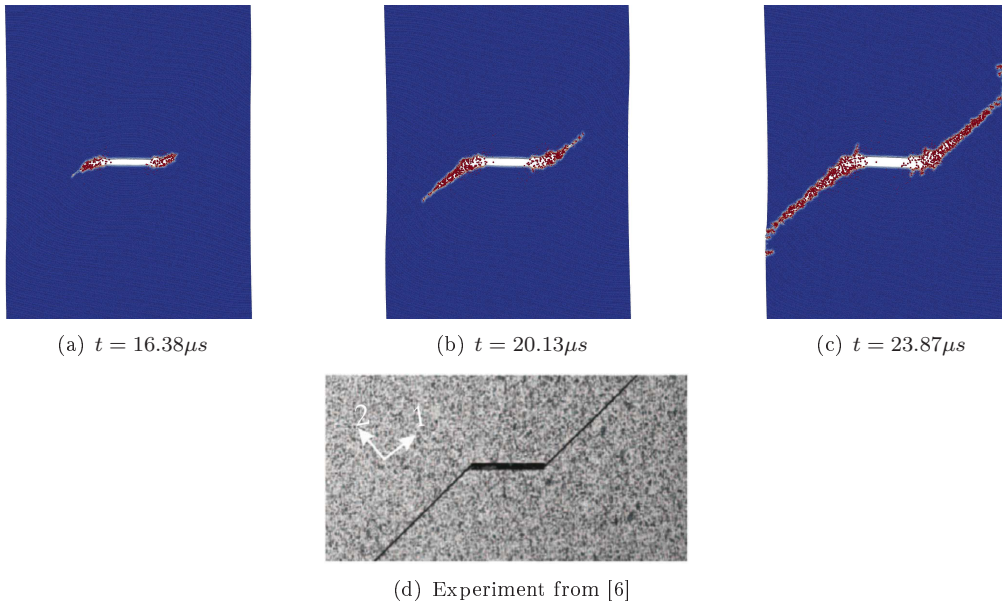
18

(a) $t = 16.38\mu s$

(b) $t = 20.13\mu s$

(c) $t = 23.87\mu s$

(d) Experiment from [6]

Figure 14: Crack propagation of centred crack for $\theta = 45^\circ$ - $m = 3$ - 300×600 particles.

(a) $t = 12.88\mu s$

(b) $t = 17.56\mu s$

(c) $t = 22.24\mu s$
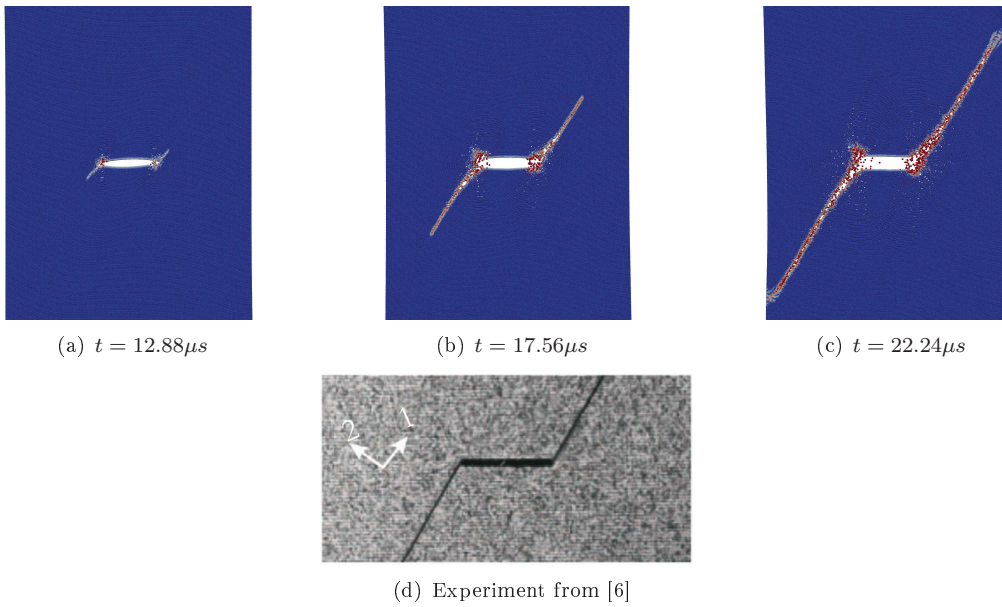
(d) Experiment from [6]

Figure 15: Crack propagation of centred crack for $\theta = 60^\circ$ - $m = 3$ - 300×600 particles.

However, since the plates are subjected to a dynamic load, some differences arise during the analysis. For instance, in Figure 13(c), some parallel cracks appear as the centred crack propagates towards
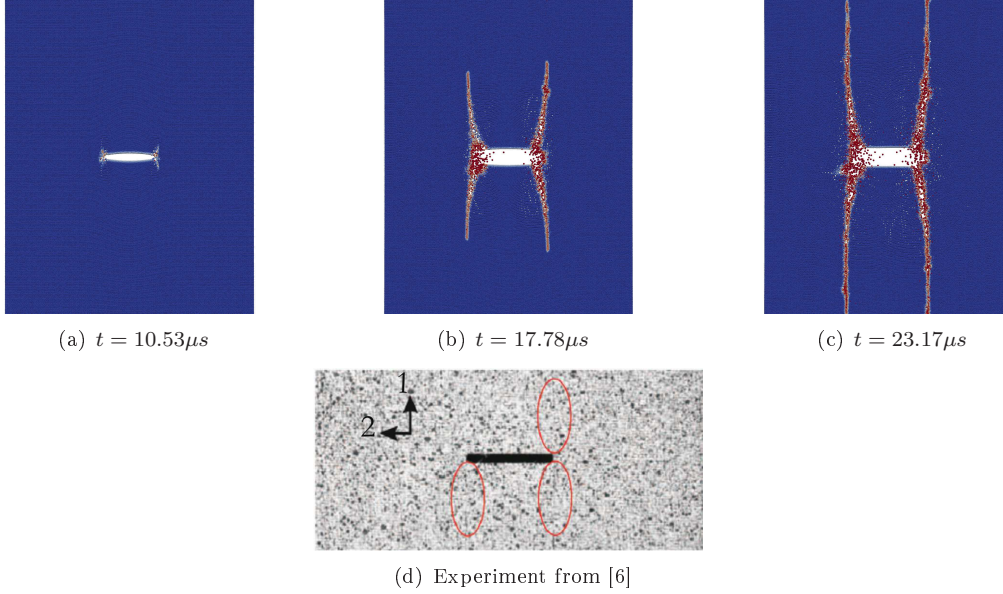
19

(a) $t = 10.53\mu s$ (b) $t = 17.78\mu s$ (c) $t = 23.17\mu s$

(d) Experiment from [6]

Figure 16: Crack propagation of centred crack for $\theta = 90°$ - $m = 3$ - 300×600 particles.

the edges of the plate. As the crack propagates, the newly formed crack surfaces increase the wave reflection inside the plate, which can lead to the formation of new cracks at the edge of the plate. Similar effects can also be seen in Figures 14(c) and 15(c), where a small level of branching appears at the crack tip as it nears the edge of the plate.

Cahill et al. [6] have mentioned that for the $\theta = 90°$ case, the crack would propagate either up or down, and occasionally it would branch. In the PD framework, we have seen that the crack always branches, propagating in both directions.

The evolution of the crack propagation for the $\theta = 60°$ fibre orientation can be visualised in the Supplemental Data available online.

6.3. Edge crack in an anisotropic plate with inclusion and hole

In this example we study a rectangular ($w = h = 20$ mm) anisotropic plate with an edge crack of length $a = 4$ mm. The plate has an inclusion of radius $r = 4.5$ mm, shifted $b = 8$ mm from the centre of the plate, and a hole of same radius shifted downwards from the centre of the plate, as illustrated in Figure 17. The plate is subjected to an initial velocity defined across the plate, and given by $v = 50\frac{y}{2h}$ m/s.

The material properties of the plate and the inclusion are given in Voigt notation by

$$\mathbf{C}^{plate}_{IJ} = \begin{pmatrix} 155.43 & 3.72 & 0 \\ 3.72 & 16.34 & 0 \\ 0 & 0 & 7.48 \end{pmatrix} \text{GPa} \tag{39}$$

$$\mathbf{C}^{inc}_{IJ} = \begin{pmatrix} 235 & 3.69 & 0 \\ 3.69 & 2 & 0 \\ 0 & 0 & 28.2 \end{pmatrix} \text{GPa} \tag{40}$$

20

FEM

- [MPa m   ]

- [MPa m   ]

Time - [s]

Time - [s]

particles

particles

particles

particles

r

θ_2

a

y

x $2b$ $2h$

PD

PD

PD

PD

PD

PD

FEM

FEM

FEM

FEM

FEM

FEM

r

θ_1

w

v

v
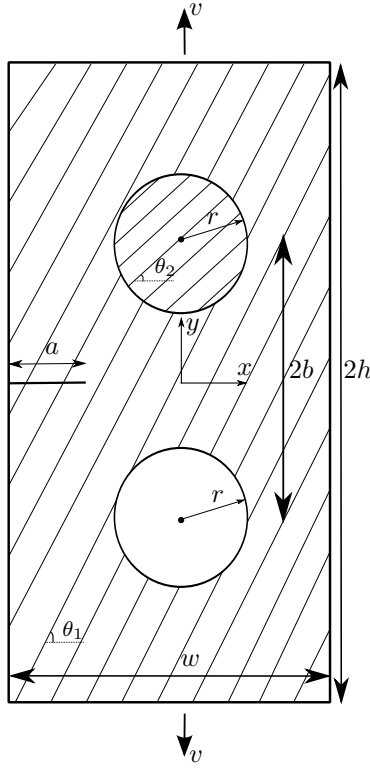
Figure 17: Anisotropic plate with inclusion and void.

The density of the plate is $\rho^{plate} = 1600$ kg/m^3 and the density of the inclusion is $\rho^{inc} = 5670$ kg/m^3. The material properties of the plate are rotated by an angle θ_1 with respect to the horizontal axis, while the inclusion represents an orthotropic material ($\theta_2 = 0°$).

Initially we study the behaviour of the problem with no crack propagation. Table 3 shows the relative error of the DSIF obtained with a finite element mesh and the PD formulation for $\theta_1 = 45°$. The finite element mesh has 165728 3-node triangular elements, and has been defined using the MESH2D algorithm (for details see reference [10]). For this configuration, the discretisation with 400×800 particles and $m = 2$ presents the lowest relative error. A possible explanation for this fact is that the horizon size is also dependent on the material properties.

In most works, it has been shown that the horizon size is chosen according to the analysed problem, however Bobaru et al. [2] have shown that the horizon size affects the dynamics of crack branching, where a horizon too large causes the elastic wave to propagate too fast, leading to differences with respect to experimental results. The influence of the horizon size in the analysis would lead to larger errors in anisotropic materials, implying that there is an optimum horizon size for a given material. For the material in the present study, Table 3 suggests that the optimum horizon size lies between Δx and $2\Delta x$.

Figures 18(a) and 18(b) depict the mode I and mode II DSIFs for this particular PD configuration, respectively. One can observe that the DSIFs calculated for different horizon sizes provide similar values of the DSIF for $n \geq 2$.

Figures 19 and 20 depict the DSIF for different values of θ. Very good agreement between the

- [MPa m   ]

- [MPa m   ]
Time - [s]
Time - [s]
particles
particles
particles
particles

Time - [s]
Time - [s]
particles
particles
particles
particles
particles
particles

Table 3: Relative error between PD and FEM for DSIF I.

Particles	Δx (mm)	$m = 1$	$m = 2$	$m = 3$	$m = 4$	$m = 5$
		Horizon $\delta = m\Delta x$				
200×400	0.10	0.8124	0.0937	0.1168	0.1227	0.1391
300×600	0.07	0.8115	0.0574	0.0751	0.0789	0.0913
400×800	0.05	0.8087	0.0487	0.0580	0.0634	0.0706

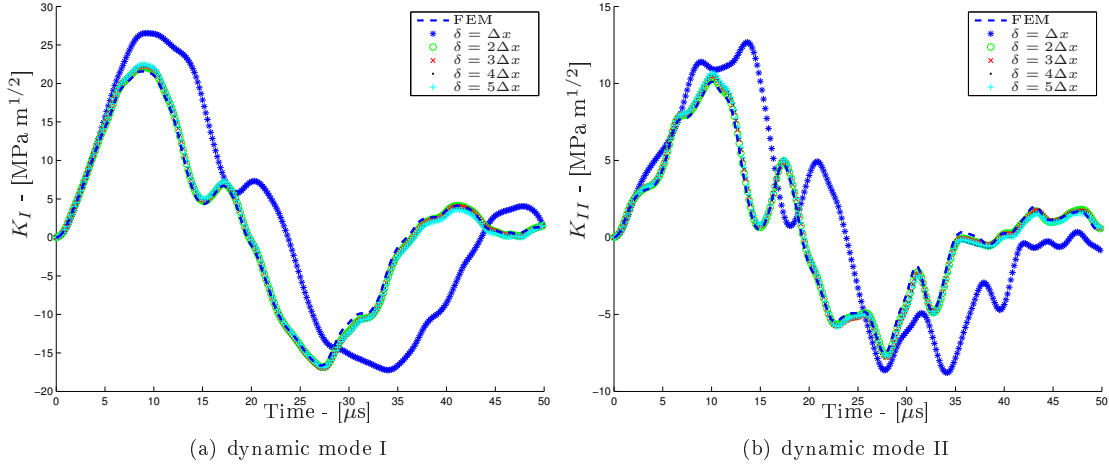(a) dynamic mode I

(b) dynamic mode II

Figure 18: Edge crack with inclusion and void: comparison between different horizon size - 400×800 particle discretisation - $\theta_1 = 45°$.

FEM and PD solutions is achieved. One can remark that the oscillation behaviour increases as θ increases, since the elastic P-wave speed in the y-direction increases with increasing θ.

370   From Figure 20, we observe that K_{II} is not zero when $\theta = 0°$ and $\theta = 90°$. Since the problem is no longer symmetric due to the presence of the inclusion and the hole, there is an acting mode II behaviour. In case where there would be a double inclusion (or double void), K_{II} will be zero for these values of θ.

Next we evaluate the crack propagation patterns in this problem. We assume the same material

375   properties given in Table 2 for the plate, while the material properties of the inclusion remain the same. The tensile strength in the fibre, matrix and shear direction of the inclusion are given by: $\sigma_{Lu} = 2100$ MPa, $\sigma_{Tu} = 120$ MPa and $\tau_{LTu} = 135$ MPa, respectively. For the interface between the plate and the inclusion, we consider the tensile strength parameters of the plate, since they assume lower values than the corresponding parameters for the inclusion. We analyse the crack

380   propagation for two different initial velocities.

Figures 21, 22 and 23 depict the crack propagation for $\theta = 0°$, $\theta = 45°$ and $\theta = 90°$, respectively, under an initial velocity of $v = 25\frac{y}{2h}$ m/s. The different orientation of the material properties provide different crack propagation paths. In Figure 21, the inclusion is not damaged, but cracks appear on the hole. From Figure 22, there is some damage arising at the interface of the plate

385   and the inclusion, as well as crack propagation from the edge crack and the hole. Figure 23 shows a different crack propagation pattern, compared to those shown in Figure 16. Additionally, the interface between the plate and the inclusion is almost fully damaged.
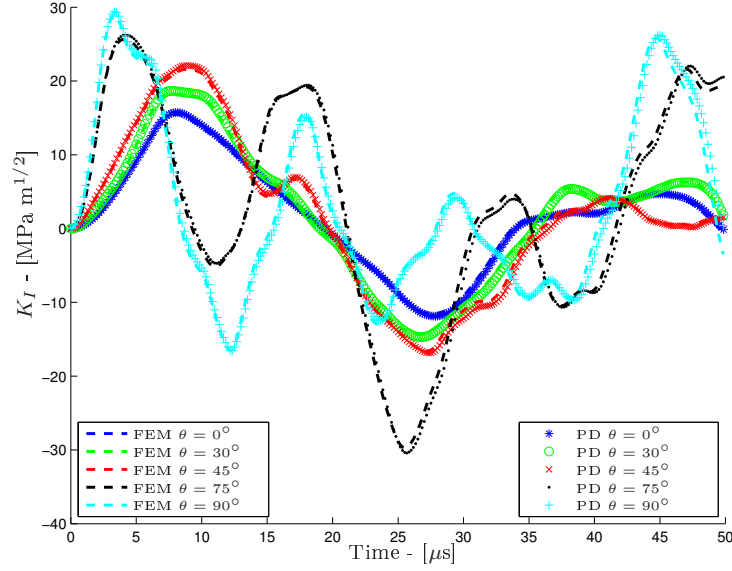
22

Figure 19: Edge crack with inclusion and void: DSIF for different values of θ - 400×800 particles - $m = 2$ - mode I.
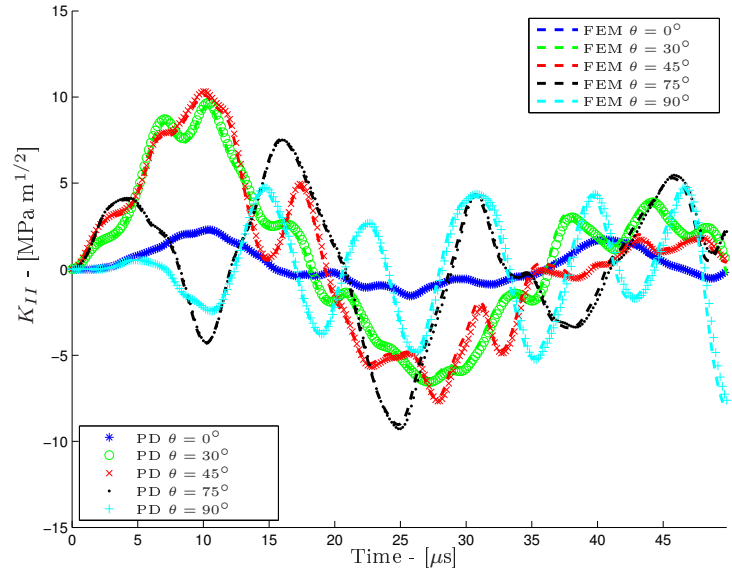

Figure 20: Edge crack with inclusion and void: DSIF for different values of θ - 400×800 particles - $m = 2$ - mode II.

Now we increase the initial velocity to $v = 50\frac{y}{2h}$ m/s and re-analyse the crack propagation for this example. The results are illustrated in Figures 24, 25 and 26. It becomes clear that the crack propagation can change depending on the loading conditions. Figure 24 now presents damage in the inclusion, and a double parallel crack originates from the hole. The crack propagation pattern
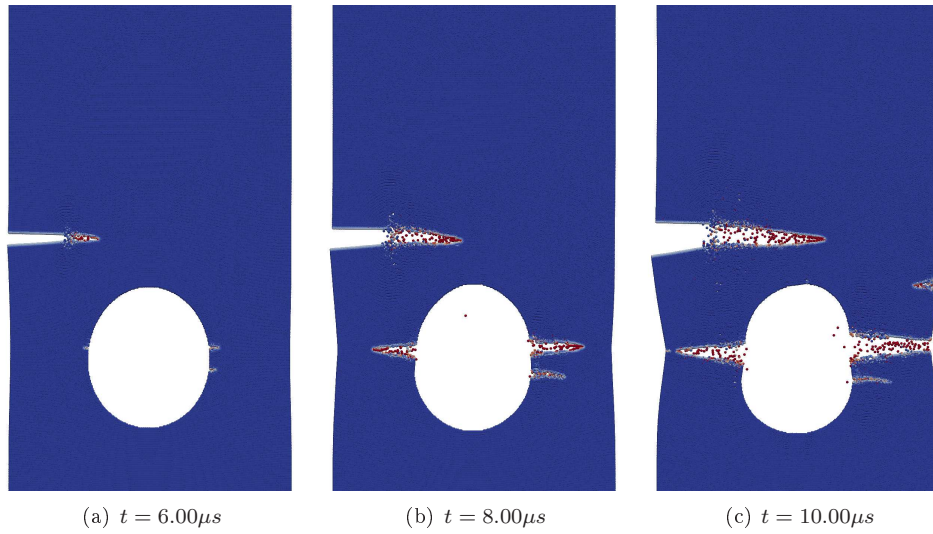
(a) $t = 6.00\mu s$ (b) $t = 8.00\mu s$ (c) $t = 10.00\mu s$

Figure 21: Crack propagation for $\theta = 0°$ - $v = 25$ m/s - $m = 3$ - 300×600 particles.

(a) $t = 4.00\mu s$ (b) $t = 9.50\mu s$ (c) $t = 13.50\mu s$
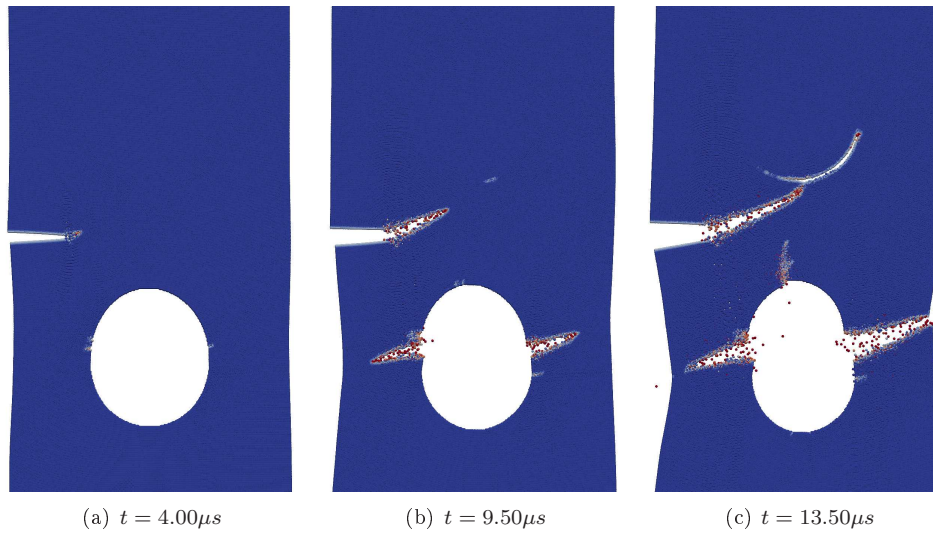
Figure 22: Crack propagation for $\theta = 45°$ - $v = 25$ m/s - $m = 3$ - 300×600 particles.

in Figure 25 is very similar to that shown in Figure 22, with the exception of the damage on the right side of the plate. Figure 26 presents an almost vertical crack propagation, reaching both the inclusion and the void. Additionally, the applied velocity is sufficiently high that some damage is

395 incurred in the inclusion.

Animations of this example for the initial velocity $v = 50$ m/s are available in the online version in the Supplemental Data section.
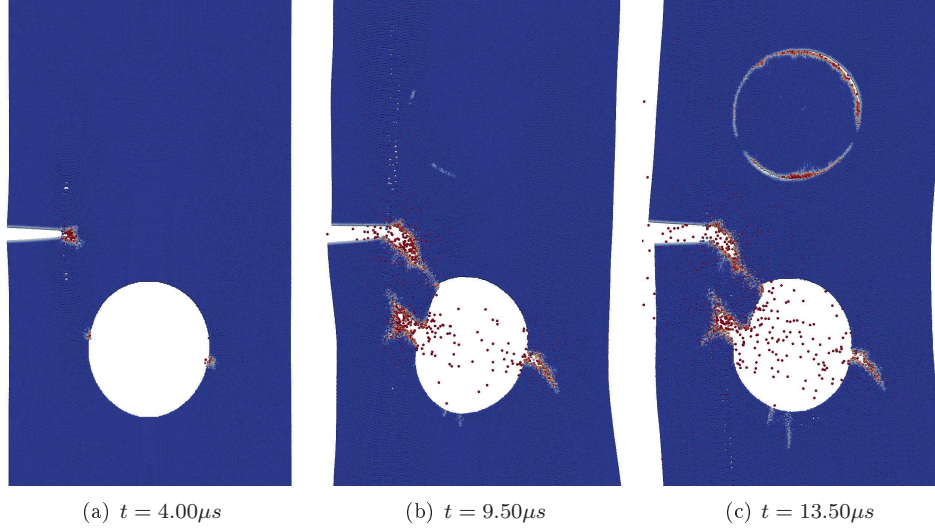
(a) $t = 4.00\mu s$ (b) $t = 9.50\mu s$ (c) $t = 13.50\mu s$

Figure 23: Crack propagation for $\theta = 90°$ - $v = 25$ m/s - $m = 3$ - 300×600 particles.

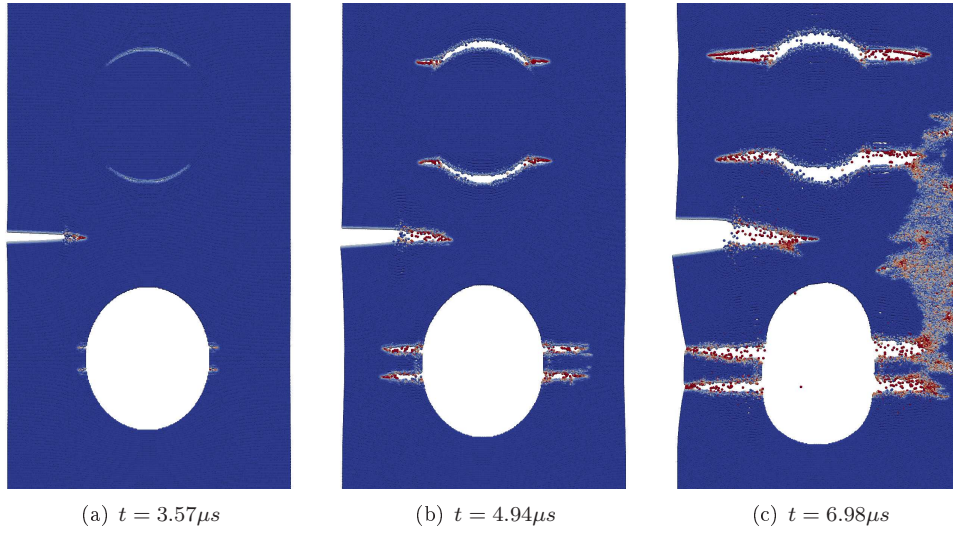(a) $t = 3.57\mu s$ (b) $t = 4.94\mu s$ (c) $t = 6.98\mu s$

Figure 24: Crack propagation for $\theta = 0°$ - $v = 50$ m/s- $m = 3$ - 300×600 particles.

6.4. Delamination between anisotropic materials

In this example we evaluate the case of a bimaterial rectangular plate with dimensions $h = 37.5$ mm and $b = 150$ mm. The interface is located at $h/2$ and contains different material properties than the other two materials. We denote material I as the material of the bottom layer of the bimaterial plate, having the same material properties given in Eq. (39) and Table 2. Material II constitutes the top layer of this plate, and its material properties are given in Eq. (40) with $\sigma_{Lu}^{II} = 2100$ MPa, $\sigma_{Tu}^{II} = 120$ MPa and $\tau_{LTu}^{II} = 135$ MPa.
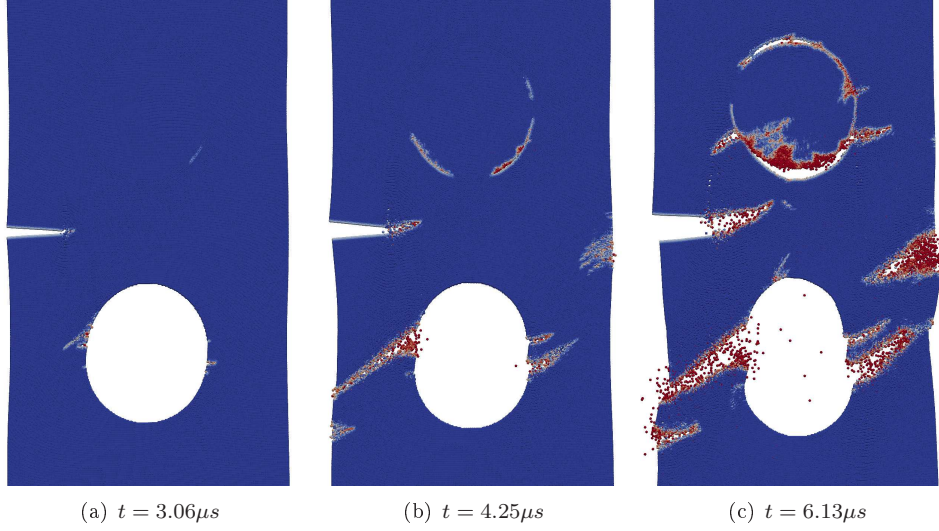
25

(a) $t = 3.06\mu s$ (b) $t = 4.25\mu s$ (c) $t = 6.13\mu s$

Figure 25: Crack propagation for $\theta = 45°$ - $v = 50$ m/s - $m = 3$ - 300×600 particles.

(a) $t = 2.04\mu s$ (b) $t = 3.40\mu s$ (c) $t = 5.44\mu s$
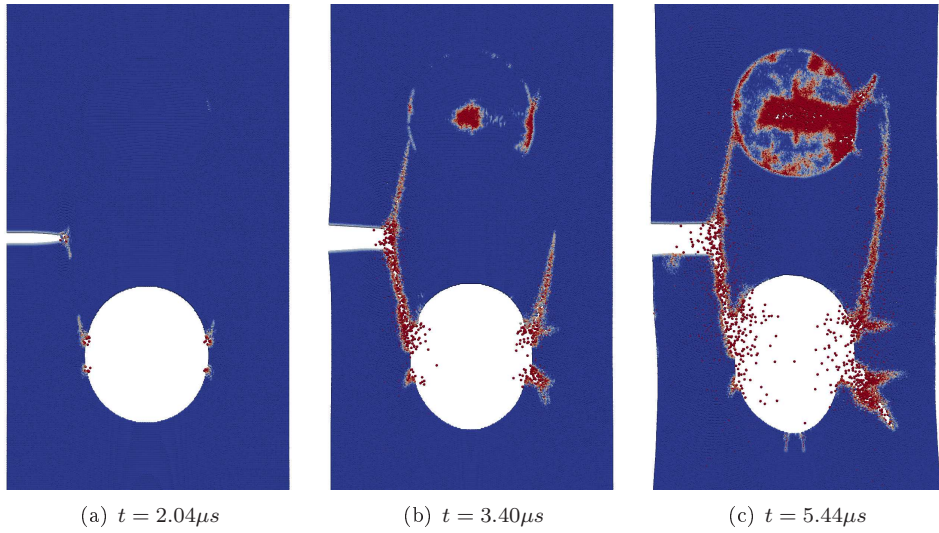
Figure 26: Crack propagation for $\theta = 90°$ - $v = 50$ m/s - $m = 3$ - 300×600 particles.

The interface of the plate is defined for every bond containing particles with two different materials. To evaluate the damage in the bonds, we assume the following parameters for failure in the interface: $\sigma_{Lu}^{int} = 1670$ MPa, $\sigma_{Tu}^{int} = 48$ MPa and $\tau_{LTu}^{int} = 56$ MPa.

In this example, we use the following parameters for the PD model: 400×100 particle discretisation, $\Delta x = 0.375$ mm and $\delta = 3\Delta x$. Analysis with these parameters has shown converged results, and increasing further the particle discretisation has a negligible influence on the results of the analysis.

26

Figure 64 depicts the plate with an edge crack of length $a = 30$ mm. Initially $d = 0$, so we study the problem with a crack at the interface. The plate is subjected to an initial velocity gradient $v = 25\frac{y}{h}$ m/s defined only on the left half of the plate ($x \leq 0$). The material properties are rotated by $\theta_I = 0°$ and $\theta_{II} = 45°$.
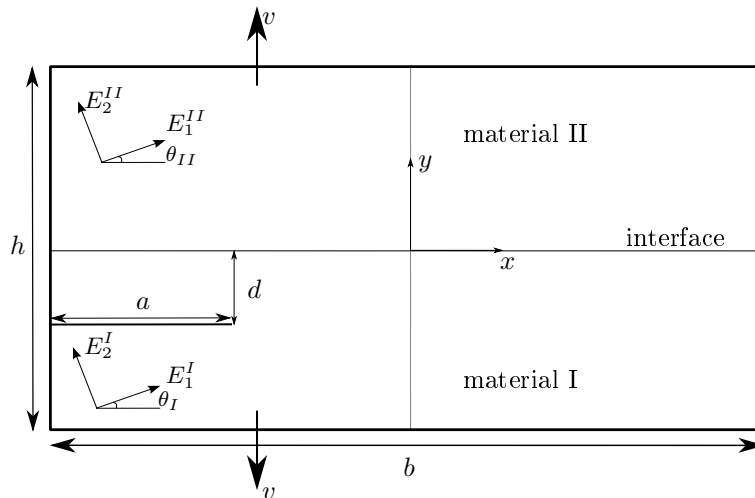

Figure 27: Delamination between two different anisotropic materials.

Figure 28 illustrates the crack propagation at several time steps. The displacements are scaled by a factor of 15. It is clear from Figure 28(b) that the crack propagates rapidly along the interface, then the crack propagation speed decreases, since the oscillatory behaviour of the plate dynamics reduces the tensile loads acting at the crack at certain times. The anisotropy of the plate combined with the dynamic effects and the formation of a new surface also lead to some damage in the top layer of the plate, as can be seen in Figures 28(c), 28(d) and 28(e).

We evaluate the delamination behaviour when the crack is no longer on the interface. The crack is shifted by a distance $d = 5$ mm and is located entirely in material I.

Figure 29 shows the crack propagation for this case. We can verify that a new crack initiates and propagates fast in the interface before that pre-existing crack propagates in material I in Figure 29(a). From Figure 29(b), the crack in material I starts to propagate, but the crack at the interface continues to propagate. The dynamic effects also cause some damage nucleation in regions of material II just above the delamination. The deformed shape illustrated in Figures 29(c) and 29(d) suggests that the delamination prevents the propagation of the crack in material I. For the investigated cases, the interface is weaker than the parent materials, which leads to the most significant crack propagation taking place at the interface. The resulting crack propagation path will depend on the relative strength of the materials and the interface.

Animations of both problems anaylsed in this section are available in the online version in the Supplemental Data section.

7. Conclusions

A generally anisotropic model for the non-ordinary state-based PD has been presented for the first time in the literature. The proposed formulation has been demonstrated for 2D materials

PSfrag replacements
FEM
- [MPa m   ]
- [MPa m   ]
Time - [s]
Time - [s]
PD particles
PD particles
PD particles
PD particles
FEM
FEM
FEM
FEM
FEM
FEM
Time - [s]
PD
PD
PD
PD
PD
FEM
FEM
FEM
FEM
FEM
FEM
Time - [s]

PSfrag replacements
FEM
- [MPa m   ]
- [MPa m   ]
Time - [s]
Time - [s]
PD particles
PD particles
PD particles
PD particles
FEM
FEM
FEM
FEM
FEM
FEM
Time - [s]
PD
PD
PD
PD
PD
FEM
FEM
FEM
FEM
FEM
FEM
Time - [s]

PSfrag replacements
FEM
- [MPa m   ]
- [MPa m   ]
Time - [s]
Time - [s]

(a) $t = 3.01 \mu s$
particles

(b) $t = 7.22 \mu s$

PD
PD
PD
particles
particles
particles
particles

PD
PD
PD
(c) $t = 15.04 \mu s$

(d) $t = 30.07 \mu s$

PD
PD
PD
FEM
FEM
FEM
FEM
FEM
FEM
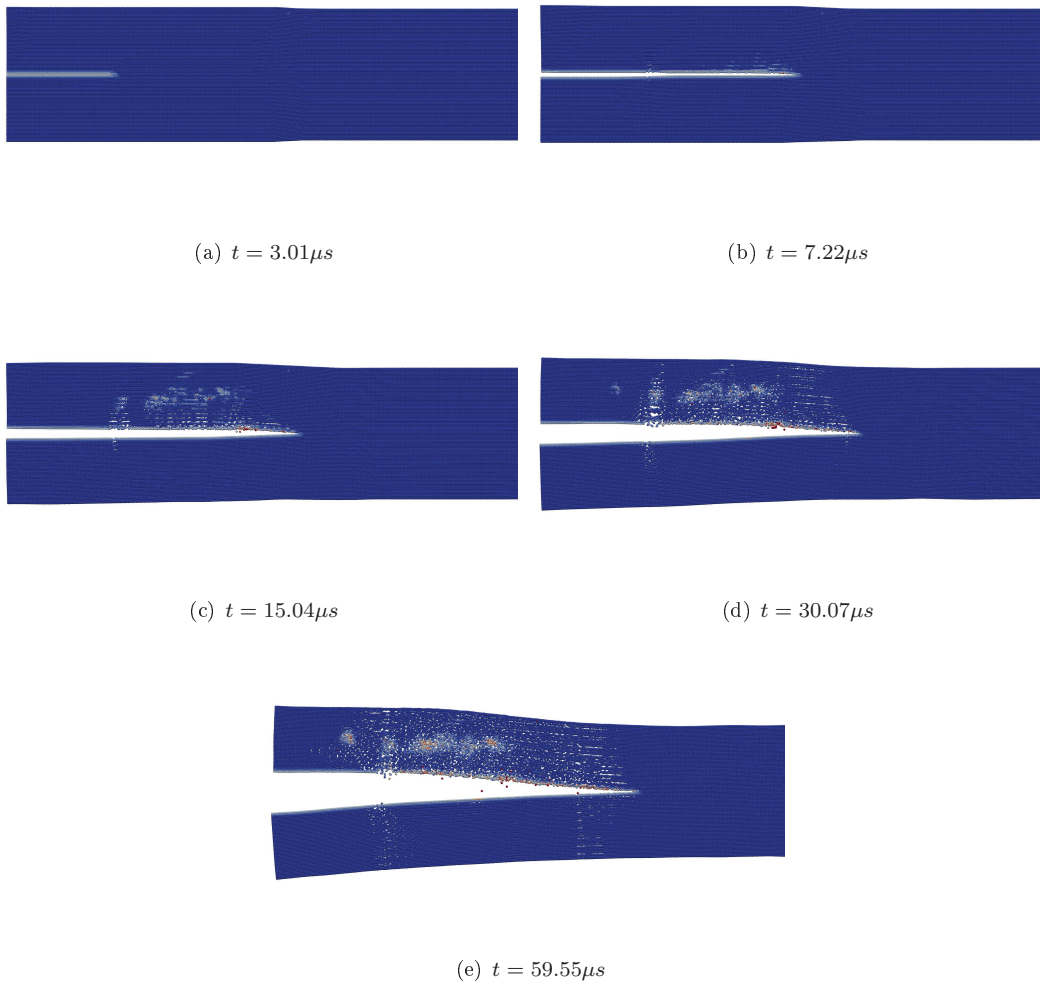Time - [s]

(e) $t = 59.55 \mu s$

Figure 28: Delamination problem with crack in the material interface.

assuming linear material behaviour and infinitesimal strains. The non-ordinary state-based framework has been used to model a composite anisotropic material. The PD formulation was validated against the FEM, and a very good agreement was achieved with both methods in the calculation of the dynamic stress intensity factors. The Tsai-Hill criterion for composite materials has been shown to provide good results for crack propagation problems. It is the first time a damage criterion for composite materials has been used in the non-ordinary state-based PD framework. It shows that different damage criteria for anisotropic materials can be employed in the future.

We have two conclusions with respect to the horizon size: in problems where the cracks do not propagate, we have shown that lower errors are achieved when $m = 2$; however, in an analysis

(a) $t = 4.81\mu s$

(b) $t = 15.04\mu s$

(c) $t = 30.07\mu s$
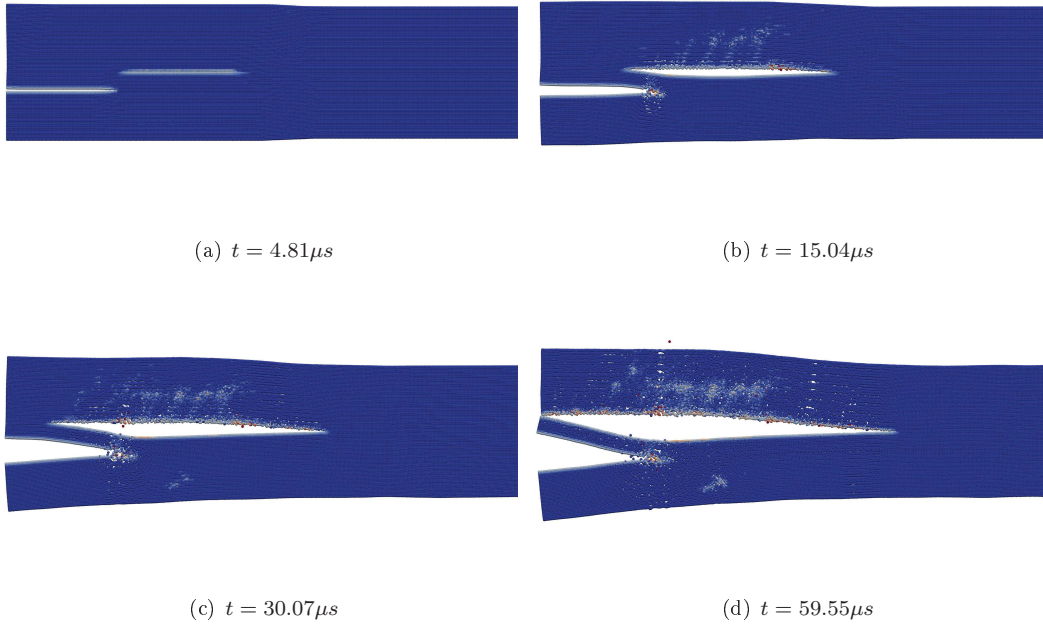
(d) $t = 59.55\mu s$

Figure 29: Delamination problem with shifted crack.

where the crack propagates, a small horizon introduces undesirable oscillations such as irregular crack paths and unexpected crack branching. This is due to the fact that material softening takes place, since the energy of the broken bonds is redistributed to the active bonds. In the case of a smaller horizon, this additional energy may be too high, and these bonds break prematurely, exaggerating the damage. Larger horizons ($m = 3$ or $m = 4$) are commonly adopted in the literature and they can stabilise the solution, since the energy of the broken bonds is redistributed over a larger number of active bonds. This shows evidence that there are optimum values of the horizon size and grid spacing in order to reduce error and to obtain a reliable analysis. So far the horizon has been chosen empirically, but it becomes evident that it also depends on the material properties. Instabilities arising from material softening for small horizons still need to be considered. The dynamic formulation has shown some interesting features for the crack propagation, where some oscillations have arisen at the edge of the plate when the crack is close to the edge. Different loading may also lead to different crack propagation patterns, especially if heterogeneities are present in the material. We have analysed delamination cases between anisotropic materials, and the results depend on the relative material properties of the interface with respect to the anisotropic materials.

The formulation can be easily extended to 3D materials and different anisotropic materials, such as rocks. In this case, a damage criterion for this specific configuration would be necessary. Future work can include the assumption of large deformation in the model. Hence, the orientation of the material will evolve with deformation. An implicit formulation can also be implemented, allowing the use of larger time steps, leading to an enhanced computational efficiency.

Acknowledgements

References

[1] Biner, S., Hu, S.Y., 2009. Simulation of damage evolution in composites: A phase-field model. Acta Materialia 57, 2088–2097.

[2] Bobaru, F., Hu, W., 2012. The meaning, selection, and use of the peridynamic horizon and its relation to crack branching in brittle materials. International Journal of Fracture 176, 215–222.

[3] Bobaru, F., Yang, M., Alves, L.F., Silling, S.A., Askari, E., Xu, J., 2009. Convergence, adaptive refinement, and scaling in 1D peridynamics. International Journal for Numerical Methods in Engineering 77, 852–877.

[4] Bouhala, L., Makradi, A., Belouettar, S., Kiefer-Kamal, H., Fréres, P., 2013. Modelling of failure in long fibres reinforced composites by X-FEM and cohesive zone model. Composites Part B: Engineering 55, 352–361.

[5] Breitenfeld, M., Geubelle, P., Weckner, O., Silling, S., 2014. Non-ordinary state-based peridynamic analysis of stationary crack problems. Computer Methods in Applied Mechanics and Engineering 272, 233–250.

[6] Cahill, L.M.A., Natarajan, S., Bordas, S.P.A., O'Higgins, R.M., McCarthy, C.T., 2014. An experimental/numerical investigation into the main driving force for crack propagation in unidirectional fibre-reinforced composite laminae. Composite Structures 107, 119 – 130.

[7] Courant, R., Friedrichs, K., Lewy, H., 1928. Über die partiellen Differenzengleichungen der mathematischen Physik. Mathematische Annalen 100, 32–74.

[8] Dipasquale, D., Sarego, G., Zaccariotto, M., Galvanetto, U., 2016. Dependence of crack paths on the orientation of regular 2D peridynamic grids. Engineering Fracture Mechanics 160, 248 – 263.

[9] Du, Q., 2017. Local limits and asymptotically compatible discretizations, in: Bobaru, F., Foster, J.T., Geubelle, P.H., Silling, S.A. (Eds.), Handbook of Peridynamic Modeling. CRC Press, Boca Raton. chapter 4, pp. 87–108.

[10] Engwirda, D., 2014. Locally-optimal Delaunay-refinement and optimisation-based mesh generation. Ph.D. thesis.

[11] Eringen, A.C., Edelen, D., 1972. On nonlocal elasticity. International Journal of Engineering Science 10, 233–248.

[12] García-Sánchez, F., Sáez, A., Domínguez, J., 2005. Anisotropic and piezoelectric materials fracture analysis by BEM. Computers & Structures 83, 804–820.

[13] Gerstle, W., Sau, N., Silling, S., 2007. Peridynamic modeling of concrete structures. Nuclear engineering and design 237, 1250–1258.

[14] Ghajari, M., Iannucci, L., Curtis, P., 2014. A peridynamic material model for the analysis of dynamic crack propagation in orthotropic media. Computer Methods in Applied Mechanics and Engineering 276, 431–452.

[15] Giordano, C., Zappalà, S., Kleiven, S., 2017. Anisotropic finite element models for brain injury prediction: the sensitivity of axonal strain to white matter tract inter-subject variability. Biomechanics and Modeling in Mechanobiology 16, 1269–1293.

[16] Giraud, A., Hoxha, D., Huynh, Q.V., Do, D.P., Magnenet, V., 2008. Effective porothermoelastic properties of transversely isotropic rock-like composites. International Journal of Engineering Science 46, 527–550.

[17] Griffith, A.A., 1921. The phenomena of rupture and flow in solids. Philosophical Transactions of the Royal Society of London A: Mathematical, Physical and Engineering Sciences 221, 163–198.

[18] Hattori, G., Alatawi, I.A., Trevelyan, J., 2017a. An extended boundary element method formulation for the direct calculation of the stress intensity factors in fully anisotropic materials. International Journal for Numerical Methods in Engineering 109, 965–981.

[19] Hattori, G., Trevelyan, J., Augarde, C.E., Cooms, W.M., Aplin, A.C., 2017b. Numerical simulation of fracking in shale rocks: Current state and future approaches. Archives of Computational Methods in Engineering 24, 281–317.

[20] Henry, H., 2008. Study of the branching instability using a phase field model of inplane crack propagation. EPL (Europhysics Letters) 83, 16004.

[21] Holzapfel, G.A., 2000. Nonlinear solid mechanics. John Wiley & Sons Ltd.

[22] Hu, W., Ha, Y.D., Bobaru, F., 2012. Peridynamic model for dynamic fracture in unidirectional fiber-reinforced composites. Computer Methods in Applied Mechanics and Engineering 217, 247–261.

[23] Hu, Y.l., Yu, Y., Wang, H., 2014. Peridynamic analytical method for progressive damage in notched composite laminates. Composite Structures 108, 801–810.

[24] Le, Q.V., Bobaru, F., 2017. Surface corrections for peridynamic models in elasticity and fracture. Computational Mechanics .

[25] Liu, W., Hong, J.W., 2012a. A coupling approach of discretized peridynamics with finite element method. Computer Methods in Applied Mechanics and Engineering 245, 163–175.

[26] Liu, W., Hong, J.W., 2012b. Discretized peridynamics for linear elastic solids. Computational Mechanics 50, 579–590.

[27] Lorentz, E., Andrieux, S., 2003. Analysis of non-local models through energetic formulations. International Journal of Solids and Structures 40, 2905–2936.

[28] Macek, R.W., Silling, S.A., 2007. Peridynamics via finite element analysis. Finite Elements in Analysis and Design 43, 1169–1178.

[29] Madenci, E., Oterkus, E., 2014. Peridynamic theory and its applications. Springer.

[30] Milazzo, A., 2012. An equivalent single-layer model for magnetoelectroelastic multilayered plate dynamics. Composite Structures 94, 2078–2086.

[31] Mossaiby, F., Shojaei, A., Zaccariotto, M., Galvanetto, U., 2017. OpenCL implementation of a high performance 3D peridynamic model on graphics accelerators. Computers & Mathematics with Applications 74, 1856 − 1870.

[32] Motamedi, D., Milani, A.S., Komeili, M., Bureau, M.N., Thibault, F., Trudel-Boucher, D., 2014. A stochastic XFEM model to study delamination in PPS/Glass UD composites: Effect of uncertain fracture properties. Applied Composite Materials 21, 341–358.

[33] Motamedi, D., Mohammadi, S., 2012. Fracture analysis of composites by time independent moving-crack orthotropic XFEM. International Journal of Mechanical Sciences 54, 20–37.

[34] Muskhelishvili, N.I., 1953. Some basic problems of the mathematical theory of elasticity. Leiden: Noordhoff.

[35] Nobile, L., Carloni, C., 2005. Fracture analysis for orthotropic cracked plates. Composite Structures 68, 285–293.

[36] Oterkus, E., Madenci, E., 2012. Peridynamic analysis of fiber-reinforced composite materials. Journal of Mechanics of Materials and Structures 7, 45–84.

[37] Oterkus, E., Madenci, E., Weckner, O., Silling, S., Bogert, P., Tessler, A., 2012. Combined finite element and peridynamic analyses for predicting failure in a stiffened composite curved panel with a central slot. Composite Structures 94, 839–850.

[38] Pensée, V., Kondo, D., Dormieux, L., 2002. Micromechanical analysis of anisotropic damage in brittle materials. Journal of Engineering Mechanics 128, 889–897.

[39] Queiruga, A.F., Moridis, G., 2017. Numerical experiments on the convergence properties of state-based peridynamic laws and influence functions in two-dimensional problems. Computer Methods in Applied Mechanics and Engineering 322, 97–122.

[40] Santiuste, C., Rodríguez-Millán, M., Giner, E., Miguélez, H., 2014. The influence of anisotropy in numerical modeling of orthogonal cutting of cortical bone. Composite Structures 116, 423 − 431.

[41] Schlüter, A., Willenbücher, A., Kuhn, C., Müller, R., 2014. Phase field approximation of dynamic brittle fracture. Computational Mechanics 54, 1141–1161.

[42] Seleson, P., 2014. Improved one-point quadrature algorithms for two-dimensional peridynamic models based on analytical calculations. Computer Methods in Applied Mechanics and Engineering 282, 184 − 217.

[43] Sih, G.C., 1991. Mechanics of fracture initiation and propagation. Springer.

32

[44] Sih, G.C., Paris, P.C., Irwin, G.R., 1965. On cracks in rectilinearly anisotropic bodies. International Journal of Fracture 1, 189–203.

[45] Silling, S.A., 2000. Reformulation of elasticity theory for discontinuities and long-range forces. Journal of the Mechanics and Physics of Solids 48, 175–209.

[46] Silling, S.A., Askari, E., 2005. A meshfree method based on the peridynamic model of solid mechanics. Computers & Structures 83, 1526–1535.

[47] Silling, S.A., Epton, M., Weckner, O., Xu, J., Askari, E., 2007. Peridynamic states and constitutive modeling. Journal of Elasticity 88, 151–184.

[48] Silling, S.A., Lehoucq, R.B., 2008. Convergence of peridynamics to classical elasticity theory. Journal of Elasticity 93, 13–37.

[49] Silling, S.A., Lehoucq, R.B., 2010. Peridynamic theory of solid mechanics. Advances in Applied Mechanics 44, 73–166.

[50] Silling, S.A., Littlewood, D., Seleson, P., 2015. Variable horizon in a peridynamic medium. Journal of Mechanics of Materials and Structures 10, 591–612.

[51] Ting, T.C.T., 1996. Anisotropic Elasticity. Oxford University Press, New York.

[52] Wang, Y., Zhou, X., Xu, X., 2016. Numerical simulation of propagation and coalescence of flaws in rock materials under compressive loads using the extended non-ordinary state-based peridynamics. Engineering Fracture Mechanics 163, 248 − 273.

[53] Warren, T.L., Silling, S.A., Askari, A., Weckner, O., Epton, M.A., Xu, J., 2009. A non-ordinary state-based peridynamic method to model solid material deformation and fracture. International Journal of Solids and Structures 46, 1186–1195.

[54] Wu, C., Ren, B., 2015. A stabilized non-ordinary state-based peridynamics for the nonlocal ductile material failure analysis in metal machining process. Computer Methods in Applied Mechanics and Engineering 291, 197–215.

[55] Wu, T.L., Huang, J.H., 2000. Closed-form solutions for the magnetoelectric coupling coefficients in fibrous composites with piezoelectric and piezomagnetic phases. International Journal of Solids and Structures 37, 2981–3009.

[56] Wünsche, M., Zhang, C., García-Sánchez, F., Sáez, A., Sladek, J., Sladek, V., 2011. Dynamic crack analysis in piezoelectric solids with non-linear electrical and mechanical boundary conditions by a time-domain BEM. Computer Methods in Applied Mechanics and Engineering 200, 2848–2858.

[57] Yaghoobi, A., Chorzepa, M.G., 2015. Meshless modeling framework for fiber reinforced concrete structures. Computers & Structures 161, 43 − 54.

[58] Zaccariotto, M., Mudric, T., Tomasi, D., Shojaei, A., Galvanetto, U., 2018. Coupling of FEM meshes with peridynamic grids. Computer Methods in Applied Mechanics and Engineering 330, 471 − 497.

[59] Zhou, X.P., Wang, Y.T., 2016. Numerical simulation of crack propagation and coalescence in pre-cracked rock-like brazilian disks using the non-ordinary state-based peridynamics. International Journal of Rock Mechanics and Mining Sciences 89, 235 − 249.